SYNTHESIS OF METAL OXIDES (Al_2O_3 AND ZrO_2) NANOPARTICLES VIA PULSED LASER ABLATION IN LIQUIDS (PLAL) AND THEIR CHARACTERIZATION USING VARIOUS ANALYTICAL TECHNIQUES

BY

FASASI TESLIM AYINDE

A Thesis Presented to the

DEANSHIP OF GRADUATE STUDIES

KING FAHD UNIVERSITY OF PETROLEUM & MINERALS

DHAHRAN, SAUDI ARABIA

In Partial Fulfillment of the
Requirements for the Degree of

MASTER OF SCIENCE

In

PHYSICS

DECEMBER, 2015

KING FAHD UNIVERSITY OF PETROLEUM & MINERALS

DHAHRAN- 31261, SAUDI ARABIA

DEANSHIP OF GRADUATE STUDIES

This thesis, written by **FASASI TESLIM AYINDE** under the direction of his thesis advisor and approved by his thesis committee, has been presented and accepted by the Dean of Graduate Studies, in partial fulfillment for the degree of **MASTER OF SCIENCE IN PHYSICS.**

M. A. Gondal

Prof. M.A. Gondal

(Advisor)

A Makki

Dr. Abdelkrim Mekki

(Member)

Dr. Saleem Rao

(Member)

Dr. Abdullah A. Al-Sunaidi

Department Chairman

Dr. Salam A. Zummo

Dean of Graduate Studies

5/1/16

Date

DEDICATION

This research is dedicated to Almighty Allah, the uncreated creator of all creatures.

I also dedicate this work to my late Father, **Fasasi Akanbi Olasupo** and my lecturer (late), Alhaji Taofeek Oyegbade-Abu Bareeroh and all deceased Muslims. May Almighty Allah forgive all their shortcomings and count them among the dwellers of Al-jannatul-firdaws. Aamin.

ACKNOWLEDGEMENTS

"In the name of Allah, the most beneficent, the most merciful"

All praises, thanks and adorations are due to Almighty Allah the most high for His mercies and blessings upon me and my family. I thank Him (Allah) for sparing my life and giving me the opportunity to complete my Master degree program successfully- Alhamdullilahi Robil-Alamin.

My sincere appreciation goes to my thesis advisor- Prof. Mohammed Ashraf Gondal for the time devoted, support, encouragement and guidance during the research work.

I will also like to appreciate my thesis committee members Dr. Abdelkrim Mekki for his constant support, assistant, cooperation, comments and understanding. May God reward you abundantly. I am also grateful to Dr. Saleem Rao for your attention, support, guidance and cooperation. I say a big thank you to you.

My appreciation goes to the Chairman, Physics Department Dr. Abdullah A. Al-Sunaidi for your cooperation and assistance. I also appreciate the efforts of my lecturers (like Dr. Z.H. Yamani, Prof. Ibraheem Naseer, Dr. Aithan, Dr. Fattah Khiari, Dr. M. Faiz, Prof. Khalil Ziq, Dr. Basheer Watheq and others) in Physics Department towards the successful completion of my master degree program in KFUPM. Thank you all.

My deep appreciation goes to my parents for their relentless effort in making me somebody in life. To my mother, I pray to Allah to give you a long life full of sound health, wealth, joy, happiness, prosperity and all good things in this life to enjoy the fruit of your labor and above all, may Allah make the word "*Lailaha ila Allahu Mohammed Rasullah*" your last word on this surface of the earth and admit you in to the highest rank of paradise. To my late Father, I pray to Allah to forgive all your mistakes while living,

count you among those with whom He (Allah) pleased with, and above all admit you into the highest level in Paradise-Aljanatul firdaws. Aamin.

To my wife and children, I really appreciate your understanding, cooperation and prayers during my MSc program. May Allah reward you immensely and may He (Allah) make the newly obtained degree beneficial to us in this world and the hereafter. Aamin.

To my brothers and sisters (The Fasasi family), I sincerely appreciate your ceaseless support and prayers during my program. May Allah reward you all abundantly. I cannot forget to say thank you to Aderoju's, Adewoyin's and Adeleke's family for their support toward my success in life. May Allah reward you all greatly.

Finally, to my friends, colleagues and well-wishers, I say "*Jazakallahu Khairan*" for your constant prayers, support and understanding.

TABLE OF CONTENTS

.

LIST OF TABLES

LIST OF FIGURES

ABSTRACT

Full Name : FASASI TESLIM AYINDE

Thesis Title : SYNTHESIS OF METAL OXIDES (Al_2O_3 and ZrO_2) NANOPARTICLES VIA PULSED LASER ABLATION IN LIQUIDS (PLAL) AND THEIR CHARACTERIZATION USING VARIOUS ANALYTICLA TECHNIQUES.

Major Field : PHYSICS

Date of Degree : DECEMBER, 2015.

Pulsed laser ablation in liquids (PLAL) is a novel technique that is capable of synthesizing colloidal solutions of nano materials. This technique is still in its infancy, and not a lot is familiar regarding this technique, neither much is known about what various conditions yield different types of materials. There are host of analytical techniques available to help us investigate the phenomena of ablation. These analytical techniques provide complimentary ideas that can be put together to obtain a picture of laser ablation in liquids. Analysis of the findings under various conditions gives us a moving picture which can tell the story of how the process works.

During the course of experimentation with ablation processes within liquid media, discovery was made that there are many parameters that can affect the output of the process. Those factors include variation in the medium of ablation, laser wavelength, irradiation time and laser fluence. In this study, variation of solvent was confirmed to affect chemical and physical properties of nano materials. The effects of annealing

temperature on the phase transformation of aluminium oxide produced were also investigated. Through investigating how different conditions affect nanomaterials properties, knowledge of the formation process is acquired and once the mechanisms involved in ablation within liquid media is understood, techniques can be applied to produce nanoparticles with tailored characteristics.

The introduction on PLAL technique and nanomaterials as well as the aim and objectives of this research are explicitly discussed in Chapter 1. Chapter 2 reviews the previous studies that have attracted great interest on the development of PLAL technique and employing it to fabricate metal oxides NPs. Detailed description of the experimental procedure involved in PLAL technique employed in this research to synthesize metal oxide NPs was presented in chapter 3. The detailed experimental procedure was provided to serve as a small encyclopedia of methods for future work to rely on. After ablation, the produced NPs were characterized by a host of techniques like XRD, SEM, FE-SEM, TEM, TGA, EDS, XPS, SAED, Uv-Vis and FT-IR. XRD provides information about the structure of the nanoparticles synthesized, SEM, FE-SEM and TEM provided great information about the morphology of our sample, EDS and XPS spectra provided elemental analysis and stoichiometric ratio of the elements present in the prepared nanoparticles. SAED helps in displaying the crystallinity of the materials while Uv-Vis and FT-IR are employed to study the optical properties of the synthesized nanoparticles. Details of these analytic techniques are elaborated in Chapter 3 of this thesis.

Experiments on aluminium (Al) and Zirconium (Zr) in chapter 4 delve into the effects of annealing temperatures on the phase transformation of alumina nanoparticles synthesized via PLAL and the effects of oxidizing media on the physical and chemical properties of

colloidal zirconia nanoparticles produce via PLAL. Lastly, Chapter 5 summarizes the whole information or results of this research and the recommendations for future research.

لخص الرمسالة

الاسم : فساسى تسليم ايديى

عنوان الرسالة: اصطناع أكاسيد المعادن (ZrO_2 ،AL_2O_3) النانوية مقابل الاستئصال بالليزر النبضى في السوائل (PLAL) ومشتقاتها وتوصيف باستخدام تقنيات ANALYTICLA المختلفة

التخصص: الفيزياء

تاريخ الدرجة العلمية : ديسمبر، 2015

الاستئصال بالليزر النبضي في السوائل (PLAL) هو تقنية جديدة قادرة على تجميع حلول الغروي (المعلقة في السوائل) من مواد النانو. هذه التقنية لا تزال في مهدها، وهناك الكثير غير مألوف بشأن هذه التقنية، لا يعرف الكثير عن أي ظروف مختلفة تسفر عن أنواع مختلفة من المواد. هناك مجموعة من التقنيات التحليلية المتاحة لمساعدتنا في التحقيق في الظواهر الاجتثاث. توفر هذه التقنيات التحليلية الأفكار المجانية التي يمكن وضعها معا للحصول على صورة من الاستئصال بالليزر في السوائل. تحليل النتائج في ظل ظروف مختلفة يعطينا صورة واضحة التي من خلالها يمكن القول عن كيفية سير الإجراءات.

خلال التجريب في عمليات الاجتثاث داخل الوسط السائل، تم اكتشاف أن هناك العديد من العوامل التي يمكن أن تؤثر على مخرجات العملية. وتشمل هذه العوامل: الاختلاف في متوسط الاجتثاث، والطول الموجي لليزر، ووقت عدم الإشعاع، وتأثير الليزر. في هذه الدراسة، تم تأكيد الاختلافات في المذيب التي تؤثر على الخواص الكيميائية والفيزيائية لمواد النانو. وأيضا تم التحقيق من آثار درجة حرارة الصلب على مرحلة التحول من أكسيد الألمنيوم المنتجة. من خلال التحقيق على كيفية التأثير على خصائص مواد النانو عند ظروف مختلفة، تم اكتساب المزيد من معرفة وفهم عملية تشكيل الآليات التي تشارك في الاجتثاث داخل الوسط السائل، وأيضا فهم العديد من التقنيات التي يمكن تطبيقها على إنتاج الجسيمات النانوية ذات الخصائص المصممة.

ناقشت مقدمة هذا البحث تقنية PLAL والمواد النانوية وكذلك الرؤية والأهداف من هذا العمل في الفصل الأول. الفصل الثاني تم استعراض الدراسات السابقة التي جذبت اهتماما كبيرا على تطوير تقنية PLAL وتوظيفها لافتعال أكاسيد

المعادن مصادر القدرة النووية. وأيضا قدم وصفا تفصيليا لإجراء التجارب المشتركة في تقنية PLAL المستخدمة في هذا البحث لتجميع مصادر القدرة النووية في أكسدة المعادن. وفى الفصل الثالث تم تقديم الإجراء التجريبي التفصيلي ليكون بمثابة موسوعة صغيرة من أساليب للعمل في المستقبل أن تعتمد على. بعد الاجتثاث، تميزت مصادر القدرة النووية التي تنتجها مجموعة من التقنيات مثل XRD، SEM، FE-SEM، TEM، TGA، EDS، XPS، SAED، الأشعة فوق البنفسجية فيس وFT-IR. يوفر XRD المعلومات حول بنية النانوية توليفها، شريطة SEM، FE-SEM وTEM معلومات كبيرة عن مورفولوجيا عينة لدينا، شريطة EDS وXPS أطياف تحليل العناصر ونسبة stiochometric من العناصر الموجودة في النانوية المعدة. SAED يساعد في عرض التبلور من المواد بينما تعمل الأشعة فوق البنفسجية فيس وFT-IR لدراسة توليف الخصائص البصرية للنانوية. وقد وردت تفاصيل هذه التقنيات التحليلية في الفصل الثالث من هذه الرسالة.

التجربة على الألومنيوم (آل) والزركونيوم (عنصر الزركون) المعادن في الفصل الرابع وأيضا تمت مناقشة آثار درجات حرارة الصلب على مرحلة التحول من الجسيمات النانوية الألومينا توليفها عبر PLAL وآثار المؤكسدة وسط المحلول على الخواص الفيزيائية والكيميائية للجزيئات النانوية زركونيا الغروية تنتج عن طريق PLAL. وأخيرا، الفصل الخامس يلخص المعلومات كاملة و نتائج هذا البحث والتوصيات في المستقبل.

CHAPTER 1

INTRODUCTION

1.1 Nanomaterials

The study of novel features of nanoparticles and their possible applications in almost every field of science including biology and medicine has become a very active area of research. The discovery of great ability of these nano particles and their potential applications in various fields is first predicted by Richard P. Feynman in his classical lecture entitled "*There is plenty of room at the bottom"* in 1959 at California Institute of Technology (Caltech) during American Physical Society annual meeting[1]. Feynman's vision was substantiated and brought to a wider audience by Eric Drexler in his book entitled "*Engines of Creation: the coming Era of nanotechnology*" which detailed the concepts and potentials of nano materials and also the hazards associated with it, if it is not properly used [2]. The word nano particle can be used to describe a large range of materials in submicron scale which include nano- and meso-scale. British Standards Institution recently suggested a definition for nano particles as the particles with one or more dimensions at the nano-scale, that is, dimensions of the order of 100 nm or less. At this level, matter develops certain novel size related properties and the materials begin to behave in a different manner compared with bulk materials [PAS71 2005]. Besides strictly nano (1-100 nm), submicron particles, that is, particles with at least one dimension in the scale 1-1000 nm called mesoscale are also regarded as nano particles and this includes organic polymer and vesicles widely adopted in the area of drug delivery[3]. At meso-scale, the characteristics of the material differ significantly from

atomic or molecular properties which are governed by laws of quantum mechanics or the properties of bulk materials determined by laws of classical physics. Therefore, the dimension of 1-100 nm is considered as an intermediate state between atomic or molecular state and bulk state where materials show anomalous characteristics that defied classical laws of physics [4]. The development of techniques such as Atomic Force Microscopy, Dynamic light scattering, Scanning Tunneling Electron Microscopy, transmission electron microscopy (TEM), high resolution transmission electron microscope (HRTEM), Scanning electron microscope (SEM), X-ray diffraction (XRD) and X-ray photoelectron spectroscopy (XPS) have contributed immensely in the characterization of nanomaterials and development in the field of nanoscience.

Metal, semi-conductor and non-metal oxides exhibit different chemical and physical characteristics as compared with that of their bulk counterparts. These novel properties of the nanomaterials are due to the quantum confinement and large surface area to volume ratio which has an inverse relationship with the size of the particle [5-7]. Thus, the wider applications of the oxides of these materials have attracted a broad interest in the synthesis of nano-structured materials having unique optical, physical, chemical and magnetic properties which are superior over those of their parent bulk materials [8].

1.2 Pulsed laser ablation (PLA)

Laser is an abbreviation which stands for “Light Amplification by Stimulated Emission of Radiation”. Stimulated emission was based on Einstein’s theory of radiation. Historically, laser was first introduced by Theodore H. Maiman on the 7th of July, 1960 when he applied ruby as a medium of laser that was stimulated via high energy flashes of

intense light. In this period of 1960, more than ten different lasers were invented using solid, gaseous, semi-conductor and also liquid media. In order to achieve optimal use of lasers and light sources as well as to carry out efficient laser treatment, a significant knowledge of lasers and light sources and basic understanding of laser physics are required. Laser has proven to be an efficient tool in various uses. A typical laser consists of a gain medium which could be solid, liquid or gas enclosed in an optical cavity and a source of energy supply (inform of electrical current or light from a flash lamp or another laser) to the gain medium. The cavity itself comprises two mirrors arranged in such a way that light bounces back and forth, each time it passes through the gain medium. The required energy for the amplification is supplied to the laser through a process called "Pumping" and the output of a laser could be a continuous constant amplitude called continuous wave (CW) or pulsed by using methods like Q-Switching, mode locking or gain switching.

A laser light consists of basically one wavelength due to fact that the emission line width is much narrower than the normal light. Another unique property of a laser light is coherence. The emitted laser light waves are in phase in time (temporal coherence) and space (spatial coherence). Laser light has high energy and it is also highly directional, it is emitted as a narrow beam and in a specific direction. This refers to as directionality. These unique properties of laser make it suitable in various applications like spectroscopy, communication, data storage, material processing, welding, induced oxidation and ablation.

The word "Laser ablation" means mass removal by coupling laser energy to a target material. Thus, pulsed laser ablation (PLA) process can therefore be defined as a process

through which material is been removed or etched from a solid surface by irradiating the solid surface with a high intense pulsed laser energy. This method (PLA) can be used for various application like elemental analysis via laser induced breakdown spectroscopy (LIBS), thin film deposition, synthesis of nanomaterials (NMs), surface cleaning and micromachining. In PLA, a high intense laser pulse energy is focused onto the surface of the sample. The process begins with the absorption of laser pulse by the target which causes the target surface to vaporize in the form of an ablation plume (as depicted in **Figure 1.1**) which contains species such as atoms, ions, and cluster travelling with high kinetic energy.

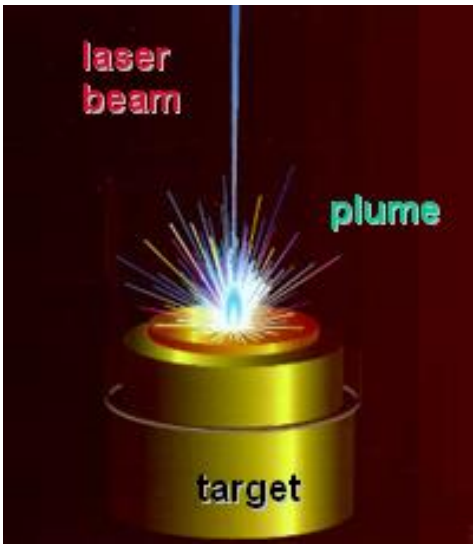

Figure 1.1: Ablation plume emission due to the vaporization of the sample surface

As a result of high intense pulse laser energy and the nanoseconds timescale, the instantaneous temperatures and pressure within the reaction volume can be extreme (many thousands of K at tens of GPa) [9]. Such high conditions of temperature and pressure provide a 'brute force' technique of synthesizing novel NMs that are yet to be achieved using milder, more conventional techniques.

1.3 Synthesis of Nanomaterials (NMs)

Synthesis of nanomaterials (NMs) with controlled morphology (size and shape) and crystalline structure is vital for the applications of nanotechnology in various fields like catalysis, medicine, and electronics. There exist many methods for synthesizing nanomaterials and these techniques are classified into two major groups which are "top-down" and "bottom-up" approach. The former involves the breaking down/ etching/division of massive or large solid into smaller and smaller portions, successfully reaching to nanometer size while the latter is a method of synthesizing nanoparticles that involves the condensation of atoms or molecular entities in a gas phase or in solution to form the material in the nanometer range. Examples of bottom-up approach are hydrothermal [10, 11], combustion synthesis [12], microwave synthesis, wet chemical route like sol-gel method and co-precipitation [13] and gas-phase technique [14, 15]. On the other hand, top-down approach involves solid state route, ball milling or attrition and pulsed laser ablation (PLA). **Figure 1.2** shows the general overview of the two approaches.

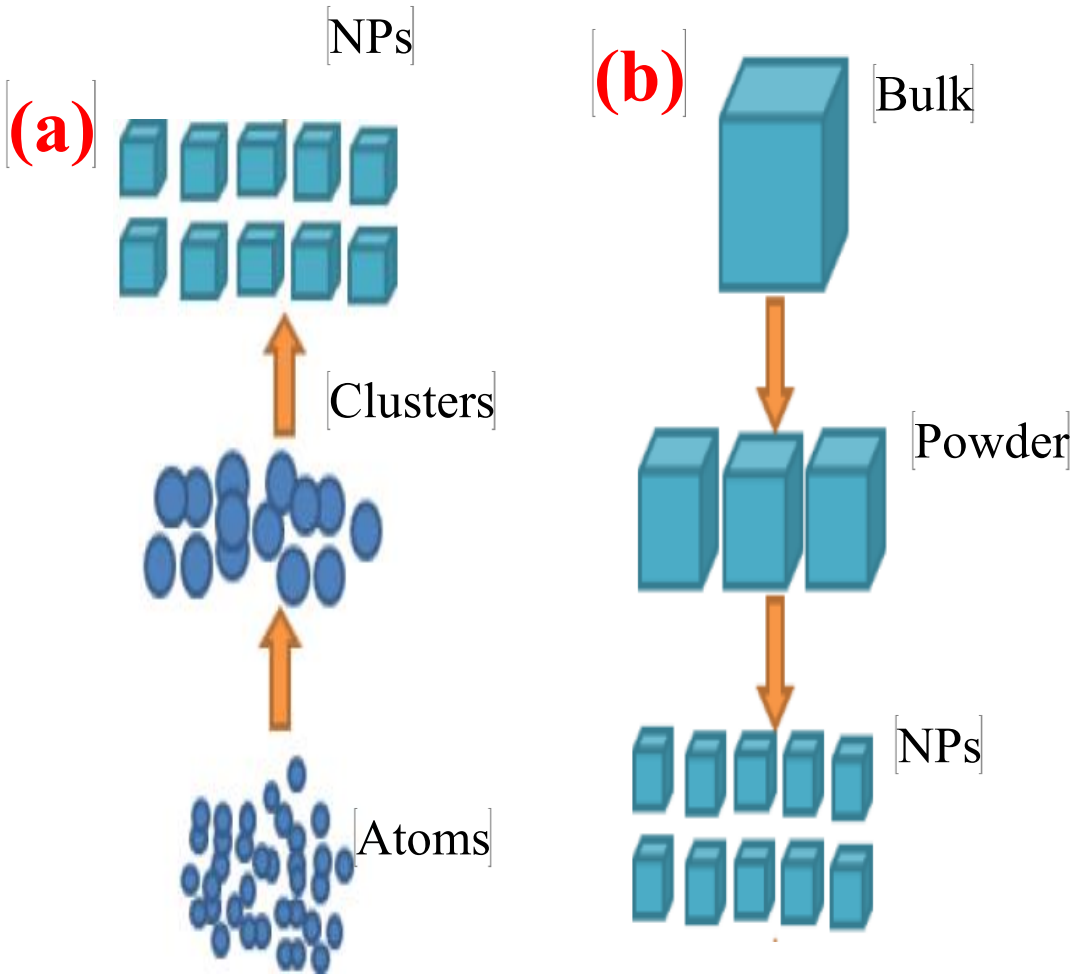

Figure 1.2: Schematic diagram of (a) Bottom-up and (b) Top-down approaches

1.3.1 Combustion route

In this process, combustion leads to highly crystalline particles with large surface area [16, 17]. The process involves a rapid heating of a solution containing redox groups [18]. During the combustion, the temperature reaches approximately 650^0C for one or two minutes to make the material crystalline.

1.3.2 Hydrothermal technique

This method is typically performed in a pressurized vessel called an autoclave with the reaction in liquid medium [19]. The temperature in the autoclave can be higher than the boiling point of water, reaching the pressure of vapour saturation. This method is widely used for the preparation of metal oxide NPs which can easily be obtained via hydrothermal treatment of peptized precipitates of a metal precursor with water [19, 20]. The hydrothermal method can be useful to regulate the grain size, particle morphology, crystalline phase and surface chemistry through regulation of the solution composition, reaction temperature, pressure, solvent properties, additives and aging time [18].

1.3.3 Microwave synthesis

This method is relatively new and an interesting method for the production of oxide nanomaterials [21]. Different NMs have been synthesized in remarkably short time under microwave irradiation [22, 23]. Microwave technique exterminate the use of high temperature calcination for long period of time and allow fast, reproducible synthesis of crystalline metal oxide NMs. Using microwave energy for the thermal treatment generally results to a very fine particle in the nanocrystalline regime due to the shorter synthesis time and a highly focused local heating.

1.4 Wet chemical synthesis

In this process, chemical reactions are applied to synthesize nanoparticles. The most common types of this process include sol-gel method, reduction method, electrochemical, hydrolysis and other precipitation techniques.

1.4.1 Sol-gel method

The sol-gel process is an effective wet chemical method to produce ceramic and glass materials. It involves the conversion of a system from a colloidal liquid (sol) into a semi-solid (gel) phase [24, 25, 26]. The sol-gel technology can be used to prepare ceramic or glass materials in a wide variety of forms: ultra-fine or spherical shaped powders, thin film coatings, ceramic fibres, microporous inorganic membranes, monolithics, or extremely porous aerogels**. Figure 1.3** below depicts an overview of the sol-gel process.

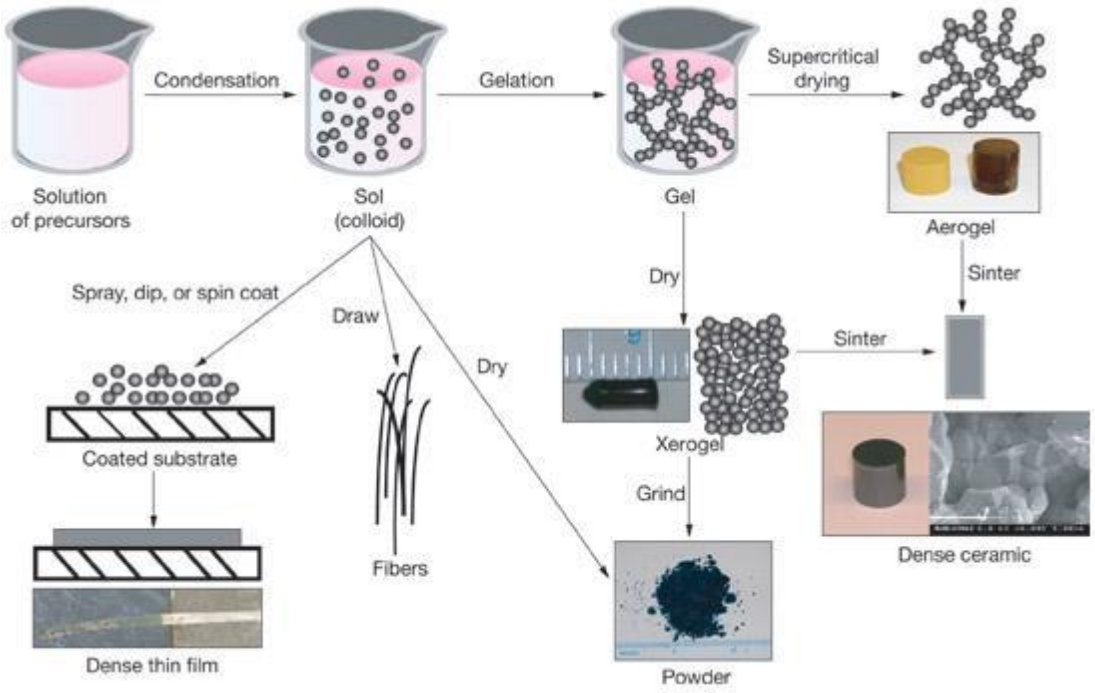

Figure 1.3: Mechanism of sol-gel process

1.5 Mechanical process

In this method, powders can be changed mechanically into smaller and smaller particle sizes. This involves grinding, milling and mechanical alloying methods.

Ball milling is a good illustration of mechanical process that is used to break massive solid into smaller and smaller portions, successively reaching the nanometer size. Materials in form of powders are crushed mechanically in rotating drums by hard steel or tungsten carbide balls. This repeated deformation can cause large reductions in grain size through the formation and organization of grain boundaries within the powder particles. Oxidation of unwanted reactions could be avoided by regulating the atmospheric conditions.

1.6 Vacuum deposition method

This method involves physical vapor deposition (PVD), chemical vapor deposition (CVD) and spray coating. Physical vapor deposition methods are atomistic deposition processes in which material is vaporized usually from a solid source in the form of atoms or molecules, transported in the form of a vapor through a vacuum or low pressure environment to the substrate where it condenses. The thickness of the deposits can vary from angstroms to millimeters. PVD process proceeds atomistically and mostly involves no chemical reaction. Generally, PVD can be divided into two groups, namely evaporation and sputtering. In evaporation, the growth species are removed from the source by thermal means. In sputtering, atoms or molecules are dislodged from solid target through impact of gaseous ions (plasma) [27].

On the other hand, chemical vapor deposition (CVD) is a chemical reaction that transforms gaseous molecules into a solid material in form of thin film or powder on a substrate. It is a widely used industrial method that can coat large areas in a short period of time [28]. In comparison with PVD, CVD has advantage of been a continuous process used for deposition, narrow size distributions and uniform coating on large areas at faster rate of deposition [29]. PVD and CVD are very similar except the form of precursor (starting material). In PVD, the precursor is in solid form whereas in CVD, the precursors are introduced into the reaction chamber in the gaseous state.

1.7 Gas phase synthesis

Gas phase synthesis includes electro-explosion and pulsed laser ablation. In electro-explosion technique, a short (microseconds) high-current and high voltage electric power impulse are applied to a high purity metal wire inside a vacuum chamber filled with gas like oxygen or argon and the conducting wire explodes into nanoscale particles. P. Sen et al applied this process to synthesize metal NPs under water using two electrodes (one in form wire and the other in form of plate). In his work, 36 V DC was used between the two electrodes. When the wire was brought into a sudden contact with the plate, it exploded into nanoscale particles. The drawbacks of this method are the complex design and it needs a high vacuum environment and high power consumption.

Pulsed laser ablation (PLA) on the other hand, is a process in which a high intense laser beam is used to irradiate the sample surface to produce nano particles. PLA can either be pulsed laser deposition (PLD) or Pulsed laser ablation in liquids (PLAL) depending on the nature of the surrounding medium during the interaction of laser beam and the

material. When ablation of material takes place in vacuum or in the gaseous medium to fabricate various thin films, it is said to be pulsed laser deposition (PLD) technique. On the contrary, when the medium of ablation is liquid, then it is called pulsed laser ablation in liquids (PLAL).

1.7.1 Pulsed laser ablation deposition (PLD)

In this method, a high power beam is focused onto a target inside a vacuum chamber as depicted in figure 4 below.

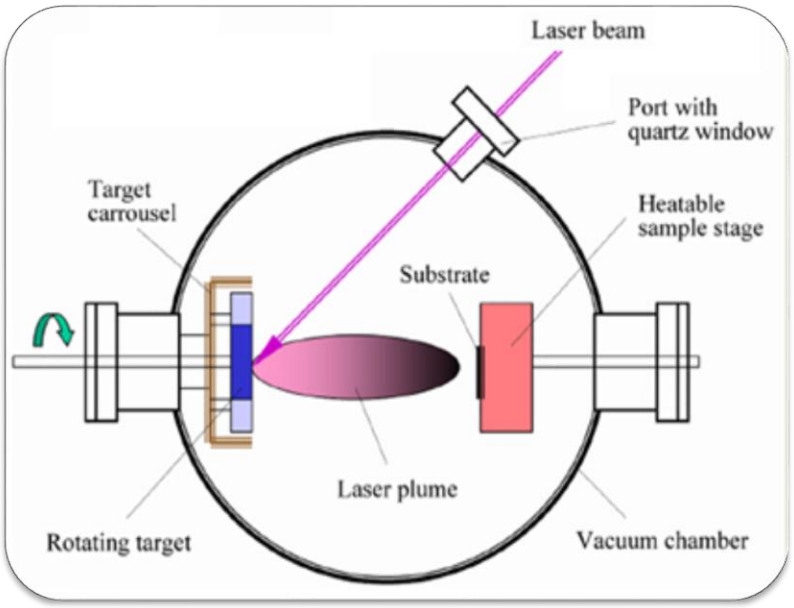

Figure 1.4: PLD experimental set-up for the synthesis of thin films

In principle, PLD is a very simple process that employs pulses of laser energy to remove material from the surface of a target, as shown schematically above. The vaporized material, containing neutrals, ions, electrons etc., is called a laser-induced plasma plume and expands rapidly away from the target surface (velocities typically ~106 cms^{-1} in

vacuum). Film growth occurs on a substrate upon which some of the plume material re-condenses. In practice, however, the situation is not so simple, with a large number of variables affecting the properties of the film, such as laser fluence, background gas pressure and substrate temperature. These variables allow the film properties to be manipulated somewhat, to suit individual applications. PLD technique has benefits over other methods like CVD, PVD and molecular beam epitaxy (MBE). With PLD, large range of ambient gas pressure is possible during film growth since the laser beam come from the outsides of the vacuum chamber and the film produced is pure because of the electromagnetic radiation (laser) used to ablate the target. Also, PLD has benefit of high speed film growth compared with other methods the technic (PLD) allows changing of the laser repetition rate, pulse energy and the distance between the substrate and the target which offers the possibility of controlling the properties of the produced thin film.

1.7.2 Pulsed laser ablation in liquids (PLAL)

The process of PLAL to synthesize NPs starts with the absorption of the laser pulse by the target (solid or powder), then a plasma plume containing the ablated materials expends into the surrounding liquid, accompanied by the emission of shock waves. During the expansion, the plasma plume cool down and releases energy into the liquid solution. This phenomenon generates a cavitation bubbles which in turn expands in the liquid and then collapses on the order of hundreds of microseconds by the emission of a second shock waves. The intermediate reactive products in the cavitation bubbles react with the molecules of the surrounding liquid and thus, produces nanostructures containing atoms from both the original target and the liquid. The confinement set up by the liquid layer together with the high temperature and pressure induced by the focused

pulsed laser beam provide an ideal environment for the formation of metastable phases and favors the synthesis of different nanostructures. This mechanism is called thermal ejection mechanism and it is the mechanism employed in this research to synthesize metal oxide nanoparticles. Another mechanism of pulsed laser ablation in liquids is explosive ejection mechanism. In this mechanism, hot nano droplets could be ejected from the target into the surrounding liquid at a very high velocity as a result of intense pulsed laser irradiation which reacts with the liquid gradually from the surface. The structure and chemical composition of the product materials are determined by the interaction of the ejected nano droplets and that of surrounding liquid which consequently depends on the nature of the medium and various laser parameters [30-33]. The target used could be metal or powder. PLAL of a powder materials dispersed in transparent liquid is used to reduce further the size of the particles into the nano scale. The choice of liquid medium, target, pulsed laser wavelength, irradiation time, pulsed laser width and pulsed laser power are the major factors contributing to the successful synthesis of nanomaterials with tailored properties. The NMs produced using this method are usually colloidal suspension or a homogenous mixture of soluble NPs and can be collected by filtration or evaporation.

PLAL is simple, versatile and does not require an expensive experimental set-up compared to other techniques. The products (NPs) obtained using this method is free of contamination and the chemicals such as surfactants can be added to liquids to control the size and aggregation state of NPs by changing the surface charge of the nuclei. Well-crystallized nanoparticles could be easily obtained in one-step without any heat treatment.

An overview of PLAL process to synthesize nanoparticles from powder target is depicted in **figure 1.5** below.

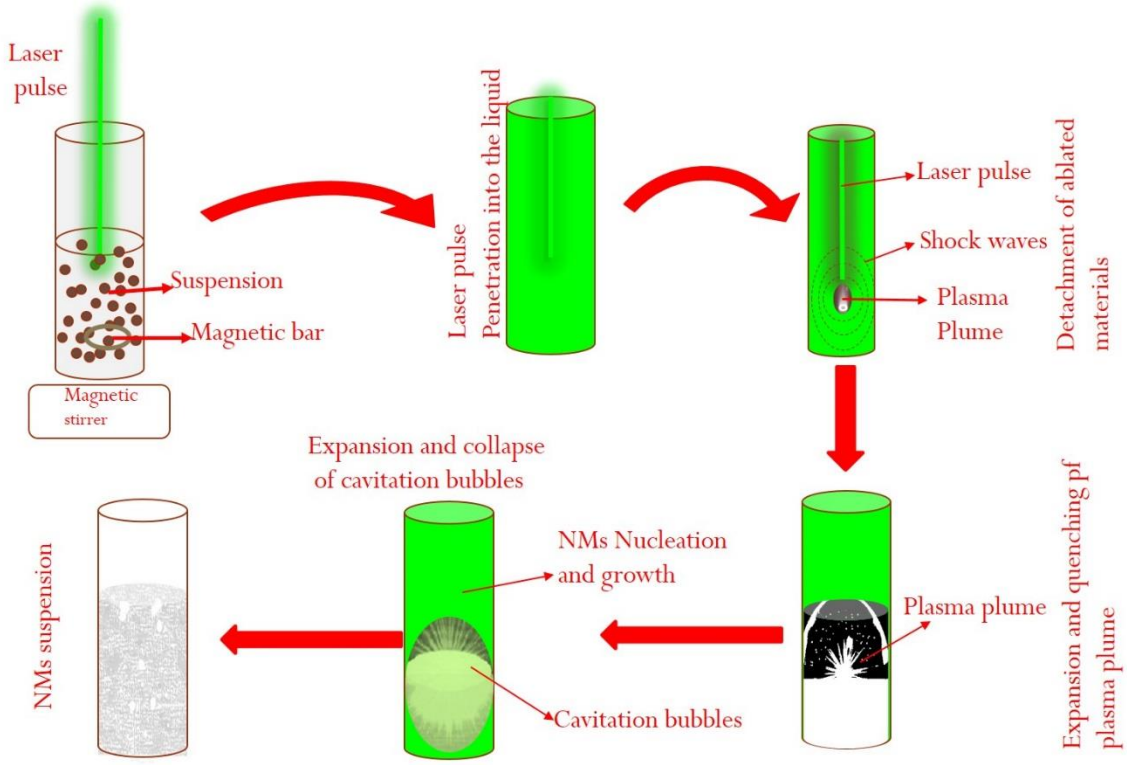

Figure 1.5: Mechanism of PLAL process to produce NPs from micro sized powder target

Laser ablation in liquid media could be generated either by nanoseconds (ns), picoseconds (ps) or femtosecond (fs) laser pulses. In this research, nanoseconds (ns) laser pulses of Nd:YAG laser of 532 nm wavelenght and the repetition rate of 10 Hz was employed to synthesize nano particles of aluminium oxide (Al_2O_3) and Zirconium (ZrO_2). The effect of annealing temperatures on the phase transition of aluminium oxide NPs and the effect of liquid media on the properties of ZrO_2 NPs were extensively studied. However, the applications of these nano-oxides (Al_2O_3 and ZrO2) were not investigated in this thesis due to the time constraints of the completion of thesis.

1.8 Aim and Objectives

The main aim of this research is to fabricate ultrafine nano structured metal oxides via pulsed laser ablation in liquids (PLAL) technique. The specific objectives are as follow:

1. Synthesis of metal oxides nano particles via pulsed laser ablation in liquids (PLAL) technique.
2. Characterization and morphological studies of the synthesized nano particles using various analytical techniques like field emission scanning electron microscope (FE-SEM), transmission electron microscope (TEM), X-ray diffraction (XRD), X-ray Photoelectron Spectroscopy (XPS), U-Vis spectroscopy, Thermo gravimetric analysis (TGA) and Fourier Transform Infrared (FTIR) Spectroscopy.
3. Study the effects of oxidizing media on the formation of nano particles from different metals like zirconium(Zr) and;

4. Study the effect of annealing temperatures on the phase transition of aluminium oxide nanoparticles (NPs).

CHAPTER 2

LITERATURE REVIEW

The main aim of this chapter is to review and summarize the previous studies which have prompted the development of PLAL technique and using it to synthesize aluminium oxides (Al_2O_3) and Zirconium oxides (ZrO_2) nanoparticles. Pulsed laser ablation (PLA) was originally invented in 1960 after the development of the pulsed ruby laser. Since then, various Scientists have been investigating laser ablation in vacuum or dilute gases. This technique can be employed to produce different kind of thin films using different target, background gases and changing parameters like laser fluence and irradiation time. These thin films could be applied in semiconductor devices, electrodes and wear resistant coatings [34].

Patil et al, 1987 reported the use of Pulsed laser ablation in liquids (PLAL) to produce metastable phases of oxides of iron using pure iron as a starting material [35]. Ogale [36] later showed that PLAL can be used to modify metal surfaces. e.g. metallixc oxidation. This earlier work on PLAL serves as an eye opener for processing materials on the basis of PLA of solids in different solvents and water. Thus, pulsed laser technique has been used to synthesize a wide range of novel materials such as nano diamond, oxides of metals and other related nanocrystals. Pulsed laser ablation has been employed to produce NPs of various kinds of metals such as zinc [37], copper [38], silver [39] and gold [40]. Also, production of compound materials nano particles like TiO_2 [41], CeO_2 [42], Tic [43], CoO [44] in

water have been reported. This method can also be used to convert structures like hexagonal boron nitride crystals to cubic boron nitride crystals [45].

Liang and co-workers first reported the synthesis of layered zinc hydroxide/dodecyl sulfate (ZnDS) structure and ZnO nanoparticles by performing laser ablation of Zn in SDS solution and pure water using the third harmonic of a Nd: YAG laser at a wavelength of 355 nm [46,47]. Using the same technique, Zeng and Co-workers prepared Zn/ZnO core/shell nanoparticles successfully by changing the laser wavelength to 1064 nm [48].

About two decades ago, Henglein reported the application of laser pulses for the synthesis of nanoparticles [49]. In his work, laser pulses were focused into a metallic target immersed in a particular liquid and the nanoparticles dispersion was obtained. Noble metals NPs are always produced via PLA due to the fact that as-prepared nanoparticles solutions do not contain any by-products and chemicals remaining from usual bottom-up approaches like chemical synthesis. So, PLA constitutes a "green" method of synthesizing nanoparticles. Several findings have been reported in the literatures about pulsed laser ablation in water and aqueous solutions of simple ions [50], organic molecules [51] or even DNA [52].

Much more development has been made recently regarding the use of PLAL to synthesize complex structures like ZnO core-shell, treelike nanostructures and silver oxide Nano dendrites. Up till now, most of the materials reported by PLAL are either continuous film structures, zero dimension (0D) NPs, or one dimension (1D) Nanorods (NRs). Since the 0D and 1D nanocrystals can serve as building blocks in producing two dimensional or three dimensional complex architectures with long

terms periodic structures. It is therefore expected that PLAL approach of synthesizing nanoparticles would be a promising method to synthesize metal oxides nanoparticles. This prompt its application in this research to synthesize Al_2O_3 and ZrO_2 nanoparticles.

2.1 Aluminium Oxides Nanoparticles

Aluminium is a vital material for several uses like additives for propellants and pyrotechnic applications [53-54]. It was reported that the use of minute particles of aluminium as fuel additives ensures the energy release in burning process and other similar systems [55-56].

Several techniques have been employed to synthesize nano sized aluminuium oxide. Different phases of aluminium oxide undergo a variety of transition until the most stable α-alumina structure is obtained at an extreme temperature [57-58]. S. Bhaduri et al [1998] and K. C. patil et al [1997] reported that for obtaining dense nano crystalline alumina products, either the phase transformation from γ to α phase has to be arrested or nano crystalline α-alumina powder have to be used. Novel nanostructured aluminas are currently employed as a support of active phases in the field of catalysis and it can coated with other materials like YAG or nano-Ni/-W to fabricate materials with extraordinary mechanical characteristics related to a very strong resistance to deformation at appropriate temperatures (YAG) or with hardness above 30 GPa (Ni, W) [59-60]. Al_2O_3 is polymorphic in nature having about seven polymorphs but only four which are $\alpha, \delta, \theta,$ and γ are usually applicable in many of the industrial operations [61]. The γ- and α- Al_2O_3 polymorphs are the nano structured phases of alumina usually synthesized via most

synthetic techniques with α-Al_2O_3 polymorph having high surface area compared with γ-Al_2O_3 polymorph [62]. The α- Al_2O_3 structure is usually referred to as corundum and it is the bulk thermodynamically stable phase with high surface area and energy compared to its γ-Al_2O_3 counterpart. The γ-Al_2O_3 has a lower surface energy and grows to energetically stable at a size below 10 nm (surface BET area ca. 75 m^2 g^{-1})[calorimetry work of McHale et al]. The surface properties of gamma phase alumina were comprehensively investigated by Knozinger and Ratnasamy[63] while Busca compiled the most recent study on surface properties of the significant alumina polymorphs like gamma and alpha[64]. Besides, new investigations confirmed that nano porosity properties affect the surface chemistry of nanostructure alumina in addition to the primary particle size [65].

The gamma polymorph undergoes a complex phase transition to alpha phase as the temperature rises. The delta alumina is usually formed in the temperature range of 973-1273 K giving off as theta phase and eventually transforms into alpha polymorphs in the temperature range of 1273-1373 K (1000^0C and above) as proved experimentally in this thesis. The $\gamma - \delta - \theta$ transition takes place systematically with thorough sintering and loss of surface area while the cubic FCC packing of the oxygen sub-lattice is maintained. This complex transformation of alumina phases has been theoretically addressed reinstating the simple fact that takes place through the movement of aluminium atom while an atom of oxygen inherently remains fixed [66].

In 2007, S. Carva et al applied polymeric precursor method to synthesize Al_2O_3 nanoparticles and investigated its phase transformation as a function of temperature.

In his work, at temperature in the range of 800-950^{0}C, pure γ-Al_2O_3 was obtained. At 1000-1025^{0}C, a mixture of α and γ-Al_2O_3 was obtained and at 1050^{0}C and above, a metastable single phase α–Al_2O_3 was obtained [67]. In 2012, Piriyawong et al performed PLAL of Al target in water which results to γ-Al_2O_3 or hydroxides [68]. Kumar et al also reported PLAL synthesis of spherical Al_2O_3 nanoparticles with an average size of 23 nm but no crystallographic phase was reported. Balaraman et al (2013) also used combustion synthesis technique to synthesize Al_2O_3 nanoparticles. In his own work, he obtained pure γ–Al_2O_3 in the temperature range of 600-875^{0}C and 900^{0}C and above, a pure α-Al_2O_3 was obtained. In this research, Al_2O_3 nanoparticles will be synthesized via PLAL techniques and its phase transition as a function of temperature will be investigated.

2.2 Zirconium Oxides (ZrO_2) Nano particles

Zirconium oxide (ZrO_2) is an oxide of a transition metal Zirconium in the periodic table with relative mass of 91.2 g/mol. It has a wide band gap around 5-5.5 eV with remarkably good mechanical, thermal, optical and electrical properties [69]. Pure zirconium oxide possesses three different crystal structure or polymorphs and each crystal structure has different densities. The three polymorphs of zirconium oxide are monoclinic (m-ZrO_2), tetragonal (t-ZrO_2) and cubic (c-ZrO_2) phases with densities of 5.6 g/cm^3, 6.1 g/cm^3 and 6.3 g/cm^3 respectively[70]. The monoclinic structure of zirconia is usually stable at room temperature and forms at the temperature range of 400^{0}C-1170^{0}C, above 1170^{0}C, it transforms to tetragonal phase. The tetragonal phase is stable up to 2370^{0}C, above this temperature results to cubic phase of zirconia which forms at the temperature range of 2370^{0}C-2600^{0}C[14] [71]. This phase

transformation of zirconia affects its density and physical features, for instance, tetragonal and cubic structure of zirconia have higher density and higher crystallization temperature compared to the monoclinic structure [72-73]. Technologically, Zirconium oxide (ZrO_2) is an excellent metallic oxide because of its outstanding properties which made it suitable as a structural ceramic, a solid electrolyte, a gas sensor, and a catalyst [74-78]. An important implication of reducing the size of pure zirconia is the likelihood of stabilizing the tetragonal phase for particles less than ca. 30nm [79]. The characteristics of the tetragonal-monoclinic transition in the nanoparticles are determined by a number of intrinsic or extrinsic factors like particle size, the pressure, potential mismatch between local and long-range order, or the presence of phase stabilizers either in the bulk (dopants) or at the surface (like water-derived or sulphate groups)[80-87]. In general, it is agreed that the tetragonal-monoclinic transformation in nanosized pure zirconia is favored upon increasing the particle size or the decreasing the pressure [88]. Zirconia nanoaprticles has better sintering behavior which made it useful as a precursor in the production of oxygen permeation membranes. Also, like other oxides, membranes formed by nanograins of stabilized zirconia have been shown to have unprecedented transport properties [88, 89].

Decreasing the size of nanoparticles can cause modification in the optical properties such as band gap by narrowing the valence and conduction bands [90]. The electronic configuration of nanomaterials is clearly different from that of bulk materials. The difference arises by systematic transformations in the density of electronic energy levels as a function of the size which results to a significant difference in the optical

and electrical properties. An increased in the band gap energy observed for particles lower than 100 nm is well explained by quantum confinement effects except for particles lower than 10 nm (quantum dot). In this case, deviations in such small size range are likely attributable to a crystalline→amorphous transition occurring for such very low size particle. Other significant factors that can determine optical band gap of nano particles are defects centers, mechanical stress and the degree of crystallinity. The variations in band gap of zirconia nanoparticles are confirmed experimentally in this work.

Micheal et al (2011) applied RAPET (Reaction under Autogenic Pressure at Elevated Temperatures) method to synthesize and characterize metallic Zr nanoparticles using MgO and ZrO_2 as the precursors [91]. In 2012, Mohammed Rafiq et al reported the synthesis of ZrO_2 nanoparticles via sol-gel technique in aqueous medium [92]. Bambang et al in 2013 also reported the synthesis of a single phase (tetragonal) ZrO_2 nanoparticles [93]. In 2014, Padovini et al applied Advance Oxidation Process (AOP)/ hydrothermal technique to produce ZrO_2 nanoparticles [94]. Adel K. Mahmoud et al in 2013 employed PLAL to synthesize ZrO_2 NPs and the medium of ablation he used was distilled water [95]. Dehzi Tan et al (2011) reported the synthesis of mixed phases of ZrO_2 (monoclinic and tetragonal) using pulsed laser ablation (PLA) in water and single phase (cubic) ZrO_2 in ammonia [69]. Synthesis of aluminium and titanium oxide nanoparticles in water, ethanol and acetone respectively via the same technique (PLAL) and the studying of the effects of these media on the size properties of the produced nanoparticles have also been reported [96]. In the present study, PLAL was employed to synthesize nanoparticles of

zirconia in three different liquid media (de-ionized water, ethanol and acetone) and the variations in the optical and other related properties of the synthesized nanoparticles were investigated. To the best of our knowledge, there is no authentic report or published data regarding the effect of oxidizing media on the properties of zirconium oxide nanoparticles synthesized via PLAL technique. Hence, this work could be regarded as pioneer work.

.

CHAPTER 3

EXPERIMENTAL SET-UP AND CHARACTERIZATION TECHNIQUES

This chapter discusses the experimental set up employed in this research to synthesize nanoparticles and the basic principles of the various analytical techniques used to perform the characterizations. Such analytical methods include X-ray diffraction (XRD) analysis, field emission scanning electron microscopy (FE-SEM), scanning electron microscopy (SEM), transmission electron microscopy (TEM), ultraviolet and visible (Uv-Vis) spectroscopy, Fourier transform infrared spectroscopy (FT-IR), x-ray photoelectron spectroscopy (XPS) and thermogravimetric analysis (TGA).

3.1 Experimental Set-Up for the Synthesis of Nanoparticles

Al_2O_3 and ZrO_2 nanoparticles were both prepared from micro-sized aluminium (Al) and zirconium (Zr) metal powder by employing pulsed laser ablation in liquids (PLAL) technique. The liquid used in case of Al_2O_3 was de-ionized water while acetone, ethanol and de-ionized water were used for the synthesis of ZrO_2. A high energy laser irradiation from a Q-Switch Nd:YAG laser (Brilliant B) working at a wavelength of 532 nm using second harmonic generator was employed as an ablation source. The laser instrument used in this project has an output of 450 mJ with a pulse width of 5 ns and works at a frequency of 10 Hz. The laser was kept at energy of 300 mJ and the focal length of 1000 mm while other parameters like pulse width and frequency were kept constant. These parameters were chosen in order to avoid laser beam travelling over a long path, thereby providing sufficient laser intensity for ablation. An approximately 0.1 g of Al and Zr metal powder were dispersed in about 15 ml of each of the liquids and irradiated with laser beam for about 60 minutes. To have uniform ablation, a magnetic bar was put in the

glass cell that contains the mixture and the glass cell was put on the stepping motor (magnetic stirrer) directly under the laser beam. The stepping motor helps to regulate the speed of the magnetic bar. Thus, the whole mixture was stirred continuously during ablation and homogenized ablation was achieved. With appropriate turning of mirror and the lens, the laser beam was routed and focused on to the sample. After 60 minutes, a white colloid was obtained in case of Al and Zr metal powder in de-ionized water but colors of colloids obtained after ablation of Zr in ethanol and acetone respectively were different. Colloids obtained in both cases were collected in a crucible and dried at a temperature of 50^0C in an oxygen atmosphere for about 5 hours to produce aluminium and zirconium oxide nano powder respectively. The produced Al_2O_3 nanopowder was further subjected to heat treatment in the furnace in the temperature range of 600^0C-1200^0C at a heating rate of 5^0 per minute for 2 hours to produce nano crystalline Al_2O_3 powder. The synthesized nano crystalline Al_3O_3 was characterized using various analytical techniques like XRD, XPS, TEM,etc. On the other hand, the produced nano crystalline ZrO_2 was used for characterization as prepared. The schematic diagram of the ablation system employed in this project for the synthesis of nanoparticles is depicted in **Figure 3.1** below:

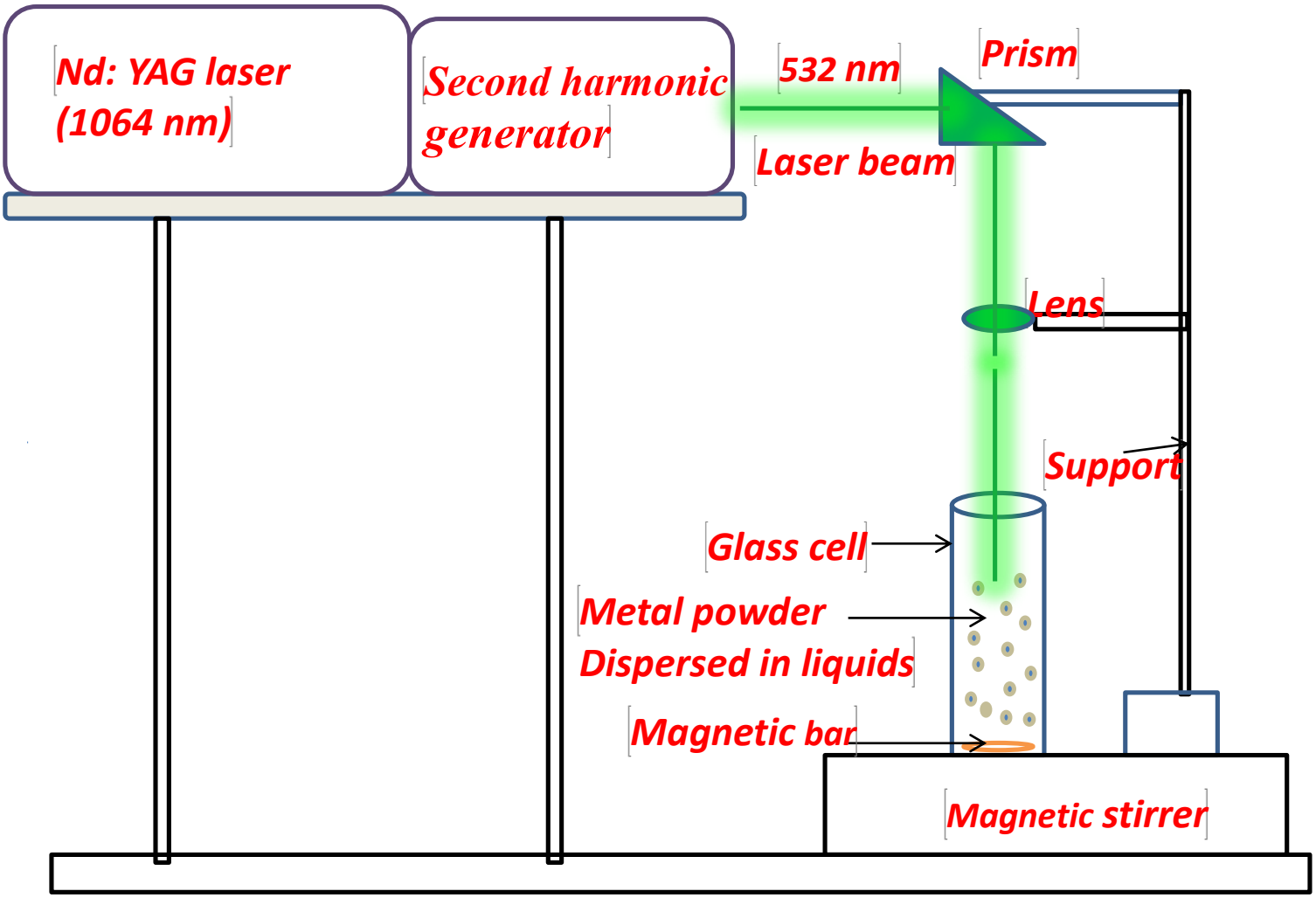

Fig. 3.1: Schematic diagram of the experimental set-up for the synthesis of nanoparticles (NPs) via pulsed laser ablation in liquids technique.

3.2 Characterization Techniques for the Synthesized Nanoparticles

The produced nano crystalline of ZrO_2 and Al_2O_3 NPs were characterized to study their properties by using X-ray diffraction spectroscopy (XRD), energy dispersive X-ray spectroscopy (EDS), field emission scanning electron microscopy (FE-SEM), transmission electron microscopy (TEM) and thermo gravimetric analysis (TGA). The optical properties of nanomaterials produced were investigated with the aid of Uv-Vis spectrophotometer and Fourier transforms infrared spectroscopy (FT-IR).

3.2.1 X-ray diffraction (XRD)

Von Laue, a German Physicist was the first who took up the problem of X-ray diffraction (XRD) in 1912 with the cause that, "*if crystals were composed of regularly spaced atoms which might act as scattering centres for X-rays, and if X-rays were electromagnetic waves of wavelength about equal to the inter atomic distances in crystals, then it should be possible to diffract X-rays by means of crystals"* [97]. Nowadays, XRD is a widely used technique for the characterization of the materials. Information like the crystalline nature of the materials, nature of the phase present in the material, lattice parameter and the grain size can be obtained from the XRD data [98]. The position and shape of the lines give certain information about the unit cell parameters and microstructural parameters like grain size, micro strain, etc. In case of thin films, the change in lattice parameter with respect to the bulk gives the information about the nature of strain present in the system.

X-ray diffraction works on the principle of Bragg's law which shows a relationship between the diffraction angles (Bragg's angle), X-ray wavelength and the inter-planar

spacing of the crystal planes. According to Bragg's law, the X-ray diffraction can be visualized as X-rays reflecting from a series of crystallographic planes as depicted in **figure 3.2** below.

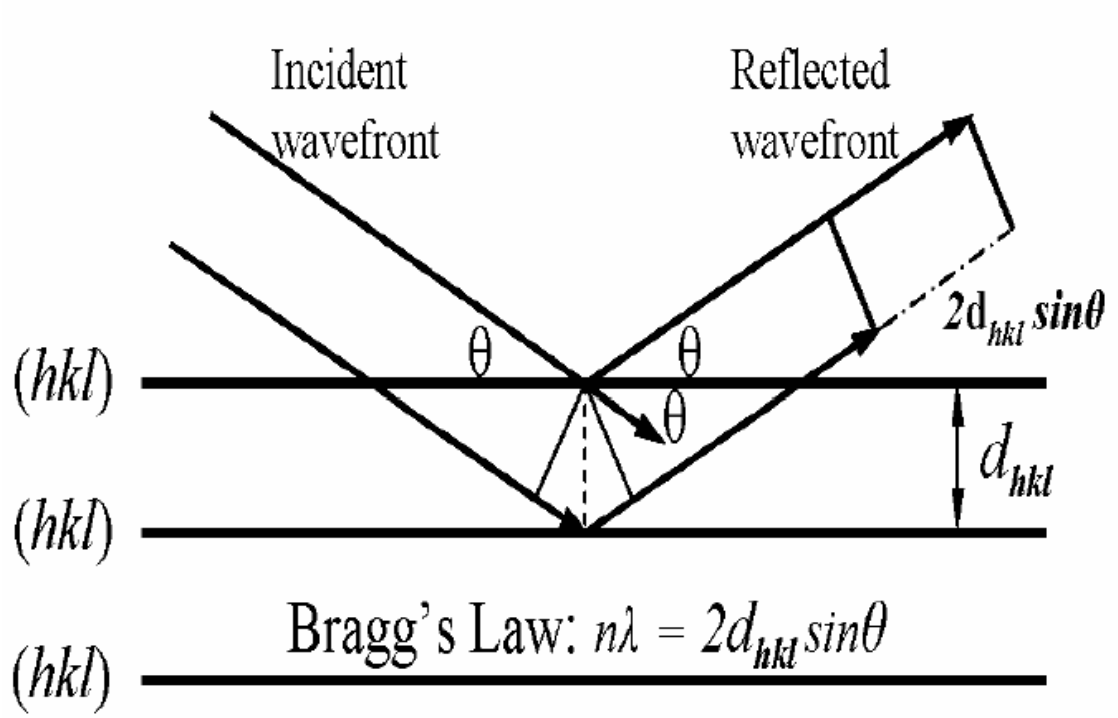

Figure 3.2: Geometrical illustration of crystal planes and Bragg's law

The path difference differences introduced between a pair of waves travelled through the neighboring crystallographic planes are determined by the interplanar spacing. If the total path difference is equivalent to nλ (n being an integer), then the constructive interference will occur and a group of diffraction peaks can be observed, which results to X-ray patterns. The quantitative account of Bragg's law can be expressed as:

$$2d_{hkl}\sin\theta = n\lambda \qquad 3.1$$

Where, d is the inter-planar spacing for a given set of *hkl* and θ is the Bragg's angle.

In this work, X-ray diffraction analysis was performed with the aid of X-ray diffractometer miniflex II from Rigaku, Japan with the following operating conditions:

- CuK_{α} (l = 1.54187Å) rdaition at room temperature from a broad focus tube at 30 kV and the filament current was 15 mA.
- Scanning speed for data collection was 3^0 min^{-1}.
- Angle scanned was in the range of 10-900 (2θ) for all samples.
- Glass was used as substrate.

X-ray diffractometer machine used for the analysis is depicted in Figure 3.3 below.

Figure 3.3: X-ray diffractometer machine employed in this research to performed XRD analysis. It is located at CENT laboratory, KFUPM, Saudi Arabia.

The phase identification for all the samples performed in this thesis was carried out by matching the peak positions and intensities in XRD patterns to those patterns in the JCPDS (Joint Committee on Powder Diffraction Standards) database.

The diffraction method is based on the effect of broadening of diffraction reflections associated with the size of the particles (crystallites). All types of defects cause displacement of the atoms from lattice sites. M.A. Krivoglaz (1969) derived an equation from the intensity of the Bragg's reflections from a crystal defect that enabled all the defects to be derived conventionally into two groups. The defects in the first group lower the intensity of the diffraction reflections but do not cause the broadening of the reflections. The reflection broadening is caused by the defect of the second group which are micro-deformations, inhomogeneity, that is non-uniform composition of the substance over their volume, and the particle size. The size of nanomaterials can be obtained from the peak broadening and can be estimated by using the Scherrer equation (3.2), provided that the crystallite size is less than 100 nm.

$$D = \frac{k\lambda}{\beta \, Cos \, \theta} \qquad 3.2$$

Where D is the average crystallite dimension perpendicular to the reflecting phases, λ is the X-ray wavelength, k is the Scherrer constant whose value depends on the shape of particles (crystallite, domain) and on diffraction reflection indices (hkl). For spherical particles for instance, it has a value of 0.9. β is the full width at half maximum (FWHM) of the peaks.

The Scherrer formula is quite satisfactory for small grains (large broadening) in the

absence of significant micro strain. A micro strain describes the relative mean square deviation of the lattice spacing from its mean value. Based on the grain size dependence of the strain, it is reasonable to assume that there is a radial strain gradient, but from X-ray diffraction, only a homogeneous, volume-averaged value is obtained.

3.2.2 Field Emission Scanning Electron microscopy (FE-SEM) and scanning electron microscopy (SEM)

Electron microscopes are simply scientific instruments which use a beam of energetic electrons to investigate objects on a very fine scale. Historically, electron microscopes were invented as a result of the limitations of Light Microscopes that are limited by the physics of light. In the early 1930s, this theoretical limit had been reached and there was a scientific need to observe the fine details of the interior structures of organic cells like nucleus, mitochondria, etc. this needs 10,000X plus magnification that was unrealistic via the existing optical microscopes.

Thus, the first scanning electron microscope (SEM) was invented and made known to the public in 1938 by Von Ardenne and the first commercial instruments was made around 1965. Its late development was due to electronics involved in “Scanning” the beam of electrons across the sample. With SEM, a highly magnified image of the surface as well as the compositional information of near surface regions of a material can be obtained [99]. Its resolution can approach a few nanometers and the magnifications of SEM can be easily adjusted from about 10 times to 300,000 times and electron beam accelerated by a relatively low voltage of 1-20 kV is scanned on the sample surface.

In this technique, the electron beam strike the surface of the sample and generate a large

number of signals from the sample surface in form of electrons or photons. The signals emitted from the sample are collected by detectors which form the images that are displayed on a cathode-ray tube screen. Basically, there are three types of images produced in SEM, namely secondary electron images, backscattered electron images and elemental X-rays maps. Secondary electrons (SE) images are considered to be the electrons resulted from inelastic scattering with atomic electrons and with the energy less than 50 eV. The secondary emission of electrons from the sample surface is usually confined to an area near the beam impact zone that permits images to be obtained at high resolution. These images as observed on a cathode ray tube, give a 3-D appearance because of the large depth of field of the SEM and also the shadow relief of the secondary electrons contrast. Backscattered electrons (BE) can be regarded as the electrons formed due to elastic scattering with the atomic nucleus and with the energy greater than 50 eV [99]. The backscattering is might occur in material with a higher atomic number so that the contrast obtained as a result of elemental differences can developed. After the primary electron beam collides with an atom in the sample and ejects a core electron from the atom, the excited atom then decays to its ground state and emit either a characteristic X-ray photon or an Auger electron [100]. The energy dispersive X-ray detector (EDX) can sort the X-ray signal by energy and produce elemental images so that the spatial distribution of particular elements can be detected by SEM. Usually, SEM has resolution of 1 nm for 1 kV, and even resolution of 0.6 nm is possible for 5 kV.

The surface morphology of samples in this theses was investigated by using SEM (JEOL JSM-6610LV scanning electron microscope) and FE-SEM (Lyra TESCAN FE-SEM)

equipped with an energy dispersive x-ray spectroscopy (EDS). The instrument is located at Center of Nanotechnology (CENT) laboratory, KFUPM and its image is depicted in **figure 3.4** below.

Figure 3.4: Schematic details of FE-SEM machine located at CENT laboratory, KFUPM, Saudi Arabia.

3.2.3 Transmission Electron Microscopy (TEM)

Transmission electron microscopy (TEM) can be defined as a microscopy technique where a beam of electrons is transmitted through an ultra-thin sample and interact with the sample as it passes through it. As a result of these interactions, a magnified image is produced and focused onto an imaging device such as fluorescent screen, on a layer of photographic film, or to be detected by a sensor such as a CCD camera. This technique is capable of imaging at a significantly higher resolution than light microscopes, due to the small de Broglie wavelength of electrons. This enables the instrument's user to investigate fine detail, even as small as a single column of atoms, which is tens of thousands times smaller than the smallest resolvable object in a light microscope. The first TEM was invented by Max Knoll and Ernst Ruska in 1931. This group developed the first TEM with resolving power greater than that of light in 1933 and the first commercial TEM in 1939.

Theoretically, the maximum resolution, d, that one can obtain with a light microscope has been limited by the wavelength of the photons that are being used to probe the sample, λ and numerical aperture of the system, NA[101]

$$d = \frac{\lambda}{2\, n \sin \alpha} \approx \frac{\lambda}{2\, NA} \qquad 3.3$$

In early 20th century, scientists theorized solutions to overcome the limitations of relatively large wavelength of visible light (wavelengths of 400-700 nm) by using electrons. Like all matters, electrons have both wave and particle properties according to Louis-Victor Ge Broglie. Their wave-like properties mean that a beam of electrons can be

made to behave like a beam of electromagnetic radiation. The wavelength of electrons is found by equating the de Broglie equation to the kinetic energy of an electron. An additional correction must be made to account for relativistic effects. In TEM, an electron's velocity approaches the speed of light, *c* [102]

$$\lambda_e = \frac{h}{\sqrt{2m_0E(1+\frac{E}{2m_0c^2})}} \qquad 3.4$$

Where, h is the Plank's constant, m_0 is the rest mass of an electron and E is the energy of the accelerated electron. Electrons are usually generated in an electron microscope by a process called thermionic emission from a filament, usually tungsten, in the same manner as a light bulb. Another way of generating electrons in an electron microscope is through the process of field emission [103]. The electrons accelerate in the presence of electric potential (measured in Volts) and focused by electrostatic and electromagnetic lens onto the sample. The transmitted beam contains information about electron density, phase and periodicity; this beam is used to form an image.

In this work, TEM images and selected area electron diffraction (SAED) of the synthesized samples were carried out by using JEM-2100F TEM machine manufactured by JEOL, USA. The image of the TEM machine employed in this research is depicted in **figure 3.5** below.

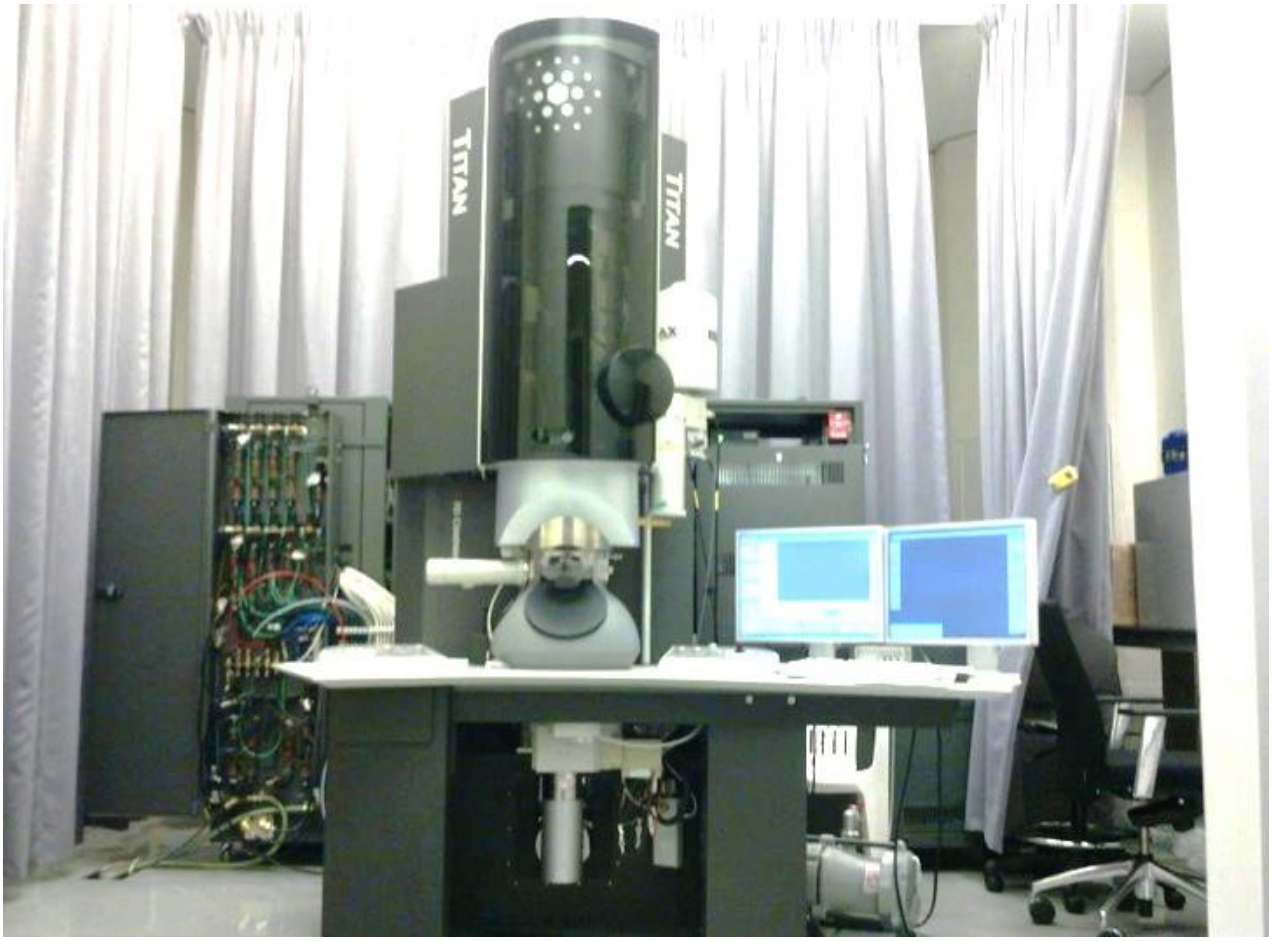

Figure 3.5: Transmission electron machine located at Material Characterization laboratory (MCL), KFUPM, Saudi Arabia.

3.2.4 Uv-Vis Spectroscopy

Ultra-violet (Uv-Vis) spectroscopy is a technique that is widely employed for the characterization of organic and inorganic man-sized molecules. In this technique, a sample is irradiated with electromagnetic waves in the Uv-Vis regions and the absorbed light is analyzed via the obtained spectrum [104, 105]. It can be applied to identify the constituents of a substance, determine their concentrations and to identify the functional groups in the molecules. The sample may be organic or inorganic and it may exist in gaseous, liquid or solid form. Various sized materials can be characterized, ranging from transition metal ions and small molecular weight organic molecules, whose diameters can be several Å, to polymers, supramolecular assemblies, nano-particles and bulk materials. Sized dependent properties can also be observed in a Uv-visible spectrum, especially in the nano and atomic scales. These include peak broadening and shifts in the absorption wavelength. Many electronic properties like band gap of a material can also be determined via this technique. The energies associated with Uv-visible ranges are sufficient to excite molecular electrons to higher energy orbitals [106, 107]. Photons in the visible region have wavelengths between 800-400 nm corresponding to energies between 1.55 and 3.10 eV. The near UV range includes wavelength down to 200 nm (6.20 eV). UV radiations of lower wavelengths is difficult to handle for safety reasons, and, is rarely used in routine UV-vis spectroscopy.

In this technique, a beam of monochromatic light is split into two beams, one of them is passed through the sample and the other passes through a reference (a solvent in which the sample is dissolved). After transmission through the sample and the reference, the two beams are directed to the detectors where they are compared. The difference between

the signals is the basis of the measurement. Liquid samples are usually contained in a cell called cuvette that has flat, fused quartz faces. Quartz is commonly used as it is transparent to both UV and visible lights.

Uv-Vis spectroscopy works on the principle of absorption of photons that promotes the molecule to an excited state; it is a suitable technique for investigating the electronic properties of nanomaterials. In the spectrum of nanoparticles, the absorption peak's width strongly depends on the chemical composition and the particle size. Consequently, their spectrum differs from their bulk counterparts. For example, for semiconductor nanocrystals, the absorption spectrum is broadened due to quantum confinement's effects [108, 102] and as their size decreases, there is no longer a distinct peak, instead there is a band. Also, semiconductor nanoparticle's absorption peaks shift towards smaller wavelengths (higher energies) as their crystal size decreases. An important consequence of using the UV-vis spectroscopy is that the band gap of Nano sized materials can be evaluated.

In this work, Uv-Vis absorption spectra of the samples were recorded with the aid of spectrophotometer (JASCO V-670) in the range of 200-800 nm. The band gap was evaluated from Tauc' relation from absorption spectra. The image of the instrument is depicted in **figure 3.6**

Figure 3.6: Uv-Vis Spectrophotometer located at laser research group laboratory, physics department, KFUPM, Saudi Arabia.

3.2.5 Fourier Transform Infrared Spectroscopy (FT-IR)

Infrared (IR) spectroscopy is a well-known method of characterization where a sample is placed in the path of an IR radiation source and its absorption of different IR frequencies is recorded [109-111]. Solid, liquid and gaseous samples can all be characterized using this method.

Basically, IR spectra are acquired by detecting changes in transmittance (or absorption) intensity as a function of frequency. This technique works on the fact that bonds and groups of bonds vibrate at characteristic frequencies. A typical FTIR comprises a beam splitter, a fixed mirror and a scanning mirror. Light from the source is divided into two parts and then recombines at the beam splitter after reflections by the two mirrors. Interference takes place as a result of the path difference between the two beams. The output beam from the interferometer is measured as a function of path difference and it sis refers to as interferogram. The IR spectrum can be obtained by calculating the Fourier transform of the interferogram. Samples can be prepared for FT-IR analysis in different ways. For powders, KBr pellet technique can be adopted. In this technique, a small amount of the sample is added to potassium bromide (KBr), after which this mixture is ground into a fine powder and subsequently compressed into a small, thin, quasi-transparent disc as depicted in **figure 3.7** below.

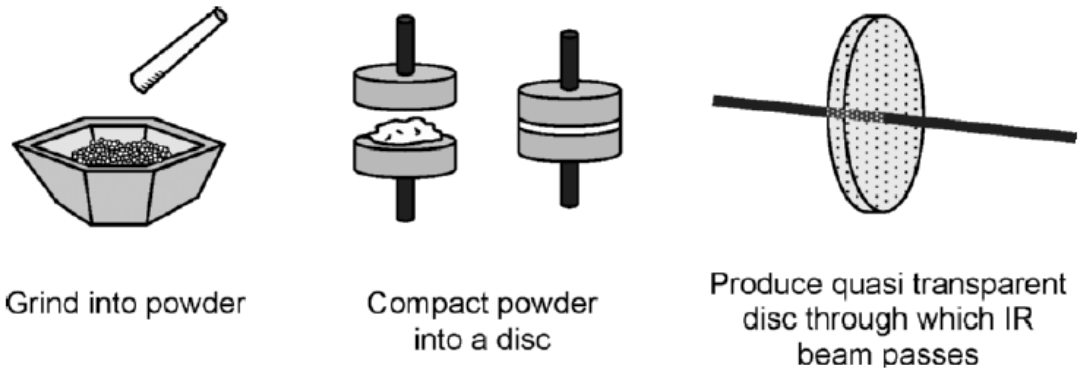

Figure 3.7: various processes in recording IR spectra

For liquid sample, a drop of sample may be sandwiched between two salt plates such as NaCl and KBr are chosen because neither of these compound shows an IR active strectch in the region typically observed for organic and some inorganic molecules.

In this work, KBr pellet technique was employed to detect the molecular structure and the presence of the functional groups adsorbed on the nano structured metal oxides synthesized via pulsed laser ablation in different liquids media. FT-IR spectra were measured and recorded with the aid of FT-IR spectrophotometer via dry KBr as standard reference in the range of 400-400cm^{1}. The image of this instrument is shown in **figure 3.8** below.

Figure 3.8: FT-IR machine located in chemistry department, KFUPM, Saudi Arabia

3.2.6 X-ray Photoelectrons Spectroscopy (XPS)

In this technique, relatively low energy X-rays are applied to eject the electrons from an atom through the process of photoelectric effects. The sample is irradiated with a beam of usually monochromatic, low-energy X-rays. Photoelectron emission results from the atoms in the sample surface and the kinetic energy distribution of the ejected photoelectrons is recorded directly via an electron spectrometer. Each surface atom has core-level electrons that are not directly involved with chemical bonding but are influenced slightly by the chemical environment of the atom. The binding energy of each core-level electron (approximately its ionization energy) is characteristic of atom and specific orbital to which it belongs. Since the energy of the incident X-rays is known, the measured kinetic energy of a core-level photoelectron peak can be related directly to its characteristic binding energy. The binding energies of the various photoelectron peaks (1s, 2s, 2p, etc) are well tabulated and XPs therefore provides a means of elemental identification which can also be quantified using measurement of integrated photoelectron peak intensities and the use of a standard set of sensitivity factors to give a surface atomic composition. The low binding energy region of the XPS spectrum is usually excited with a separate ultraviolet photon source, such as a helium lamp, ultraviolet photoelectron spectroscopy (UPS) and provides data on the valence band electronic structure of the surface [112]. An illustration of photoelectron emission in XPS analytical technique is depicted in **figure 3.9** below.

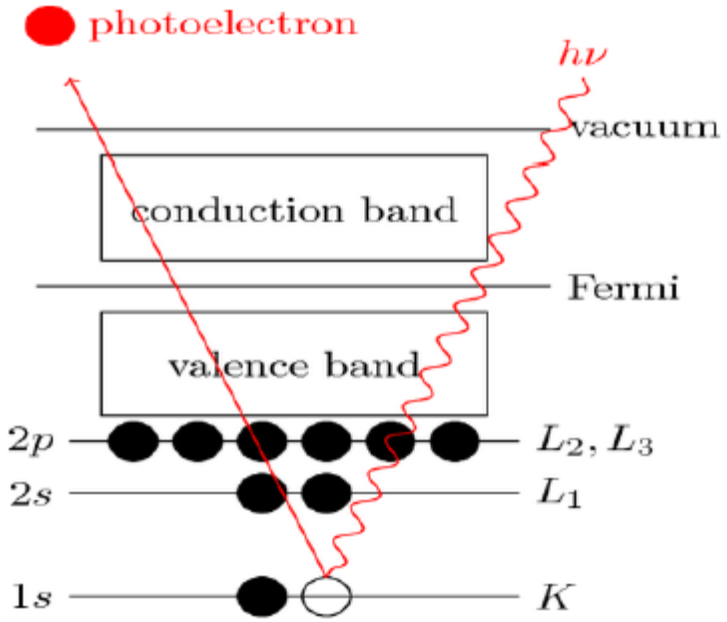

Figure 3.9: Schematic of photoelectron emission in XPS technique

In this research, survey scans and high resolution core level spectra of the various constituents of the nano structured metal oxides synthesized were recorded using Thermo Scientific Esccalab 250Xi spectrometer. Monochromatic Al Ka radiation of energy 1486.60 eV was employed as our X-ray source in this research. The spectra were referenced with the adventitious C 1s peak at 284.6 eV. The resolution of the instrument was 0.5 eV and the analysis chamber was kept at a base pressure of 5 x 10^{-10} mbar. Pass energy of 100 eV was used for survey scans while 20 eV was used for high resolution scans. A flood gun was used to compensate for surface charging and the sample was subjected to Ar^+ ion bombardment for about 90 s to clean the sample from surface contamination. The image of the instrument is depicted in **figure 3.10** below

Figure 3.10: X-ray photoelectron spectrophotometer located at surface science laboratory, physics department, KFUPM, Saudi Arabia.

3.2.7 Thermo gravimetric analysis (TGA)

Thermogravimetric analysis (TGA) is an analytical technique employed to investigate a material's thermal stability and its fraction of volatile components by monitoring the weight change that occurs as a specimen is heated. The measurement is normally carried out in air or in an inert atmosphere, such as Helium or Argon, and the weight is recorded as a function of increasing temperature. Sometimes, the measurement is performed in a lean oxygen atmosphere (1 to 5% O_2 in N_2 or He) to slow down oxidation. In addition to weight changes, some instruments also record the temperature difference between the specimen and one or more reference pans (differential thermal analysis, or DTA) or the heat flow into the specimen pan compared to that of the reference pan (differential scanning calorimetry, or DSC). The latter can be used to monitor the energy released or absorbed via chemical reactions during the heating process.

In this study, thermo-gravimetric analysis (TGA) was carried out using a thermal analyzer SDT Q600, V20.9 Build 20 manufactured by TA instruments, USA. The temperature was raised at a uniform rate of 10^0c/min. the analyses were made over a temperature range of 20-800^{0}C in an air-atmosphere flowing at a rate of 100 mL/min. The instrument is located in chemistry department, KFUPM, Saudi Arabia.

CHAPTER 4

RESULTS AND DISCUSSION

In this chapter, results and detailed discussion with respect to the synthesis of metal oxides (Al_2O_3 and ZrO_2) by employing PLAL technique are elaborated. The morphological, compositional, structural, thermal and other related properties like optical are also presented.

4.1 Effect of Annealing Temperatures on the Phase Transition of Al_2O_3

In this section, the synthesis of nano crystalline Al_2O_3 via PLAL method is explicitly stated. The effect of annealing temperatures on the phase transition of the synthesized aluminium oxide NPs is critically examined as presented in the following subsections:

4.1.1 Synthesis of Al_2O_3 Nanoparticles

The experimental set-up shown in **Fig. 3.1** was utilized for the synthesis of Al_2O_3 nano particles. When a high energy laser beam irradiates the micro-sized Al powder which was dispersed in de-ionized water, most of the laser beam was absorbed by the target (Al metal powder) which consequently results to melting, vaporization, atomization and ionization of Al powder. As a result of high intense laser beam, a chemical reaction occurs between Al metal and water and thus, produces white colloid of aluminium oxide nanoparticles which was collected and dried in an oxygen atmosphere for about 5 hours to obtain whitish nano crystalline aluminium oxide powder. The obtained Al_2O_3 nanopowders were further heated at various temperatures to investigate the phase transformation behavior of Al_2O_3.

4.1.2 Structural Characterization of Al_2O_3 Nano particles (NPs)

The X-ray diffraction (XRD) pattern of the starting material (Al powder) is depicted in **Figure 4.1 (a)** with diffraction peaks at 2θ,38.5^0 for (111), 44.7^0 for (200), 65.10 for (220), 78.2^0 for (311) and 82.4^0 for (222) [JCPDS No. 00-04-0787] indicating the presence of aluminium metal.

Figure 4.1 (b) depicts XRD pattern of as-prepared nano crystalline Al_2O_3 powder which indicates the formation of γ-Al_2O_3 and Aluminium hydroxide Al $(OH)_3$. The diffraction peaks at 2θ, 20.5^0 for (111), 37.6^0 for (311), 40.0^0 for (222), 45.9^0 for (400), 67.0^0 for (440)[JCPDS No. 10-0425] confirm the formation of $\gamma - Al_2O_3$ phase and diffraction peaks at 18.5^0 for (002), 47.6^0 for (402), 53.1^0 for (124), 63.9^0 for (51-3)[JCPDS No. 01-074-6632] confirm the formation of aluminium hydroxide Al $(OH)_3$. This finding is in good agreement with the literature [68].

Figures 4.1 (c) - (h) depict the XRD patterns of the annealed nano crystalline powder obtained in the temperature range of 600^0C-1200^0C. At 600^0C, as-prepared Al_2O_3 which is a mixture of γ-Al_2O_3 and Al $(OH)_3$ transformed to pure γ-Al_2O_3 and up to 900^0C, the pure γ-phase of Al_2O_3 was obtained. This can be compared with transformation temperature in the range of 600 to 900^0C, with low intensity which confirmed the transformation of mixed phases of alumina to pure γ-phase alumina. At 1000^0C, the degree of crystallinity was considerably increased as temperature increased. At this stage, pure γ-Al_2O_3 was completely transformed to a stable single-phase α-Al_2O_3 with the crystallite size increased as the temperature increases. **Figure 4.1 (g)** and **(h)** depict XRD pattern of nano crystalline alumina powder annealed at 1000^0C and 1200^0C respectively

with diffraction peaks at 2θ, 25.6^0 for (012), 35.2^0 for (104), 46.2^0 for (202), 52.6^0 for (024), 59.7^0 for (211), 74.30 for (208), 80.40 for (217) [JCPDS No. 04-0787] indicating the formation of α-alumina. In these range of temperatures, 1000^0C and above, no more appearance of other phases could be found except α-Al_2O_3. This confirms that at 1000^0C and above, transformation of pure γ-Al_2O_3 to a single-phase α-Al_2O_3 has taken place.

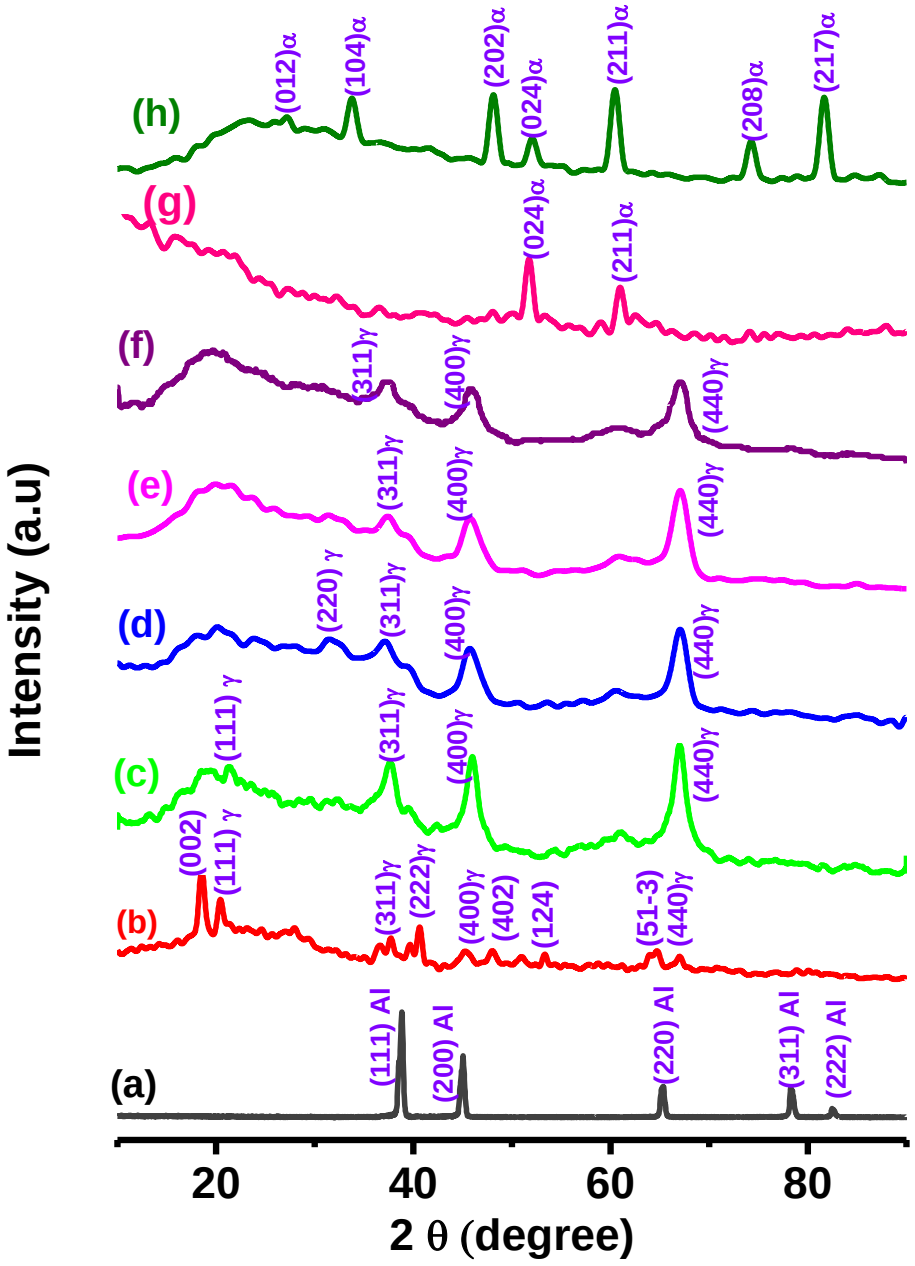

Fig. 4.1: X-Ray Diffraction (XRD) pattern of: (a) Original (bulk) Aluminium powder ; Nano crystalline Al_2O_3 (b) As- prepared ; Nano crystalline Al_2O_3 annealed at (c) 600^0C ; (d) 700^0C (e) 800^0C (f) 900^0C (g) 1000^0C (h) 1200^0C for 2 hrs respectively.

The average crystallite size of Al_2O_3 was obtained using Scherrer formula [42] as indicated in **Table 4.1** below.

Table 4.1: Phase Structure and Crystallite Size of nano crystalline Al_2O_3 as-prepared and annealed at various temperatures

S/No	Annealed Temperature (^{0}C)	Crystallite Size (nm)	Phase Structure	Plane (hkl)
1	600	7.02	γ	(440)
2	700	6.25	γ	(440)
3	800	5.30	γ	(440)
4	900	9.34	γ	(440)
5	1000	26.40	α	(211)
6	1200	36.35	α	(211)

From 600^{0}C on, crystallite size of the samples decreases with increase in the annealing temperature, until it reaches the threshold value at 800^{0}C. This is as result of the crystallization of γ-phase, whose particles are typically ultrafine. As γ-Al_2O_3 transforms to α-Al_2O_3 phase, the particle size increases, meaning that the gaps between the chains and crystal defects are gradually reduced and eventually disappear along with the crystallization of α-Al_2O_3 phase. The similar increases in crystallite size along with the formation of α-alumina have been reported for Al_2O_3 nanopowder obtained via other techniques [113-114]. It should be noted that in the temperature range of 600-900^{0}C where there are 100% γ-Al_2O_3, the crystallite size is small, less than 10 nm. This is in a good agreement with the works of McHale et al [115]. The peak corresponding γ- Al_2O_3

phase (440) in as-prepared sample is almost amorphous with a size of 3.9 nm. At 1000^0C, the crystallite size reached 26.40 nm where all $\gamma-Al_2O_3$ is transformed to α-Al_2O_3. A sketch of the observed phase transitions as function of temperature is depicted in **Figure 4. 2**

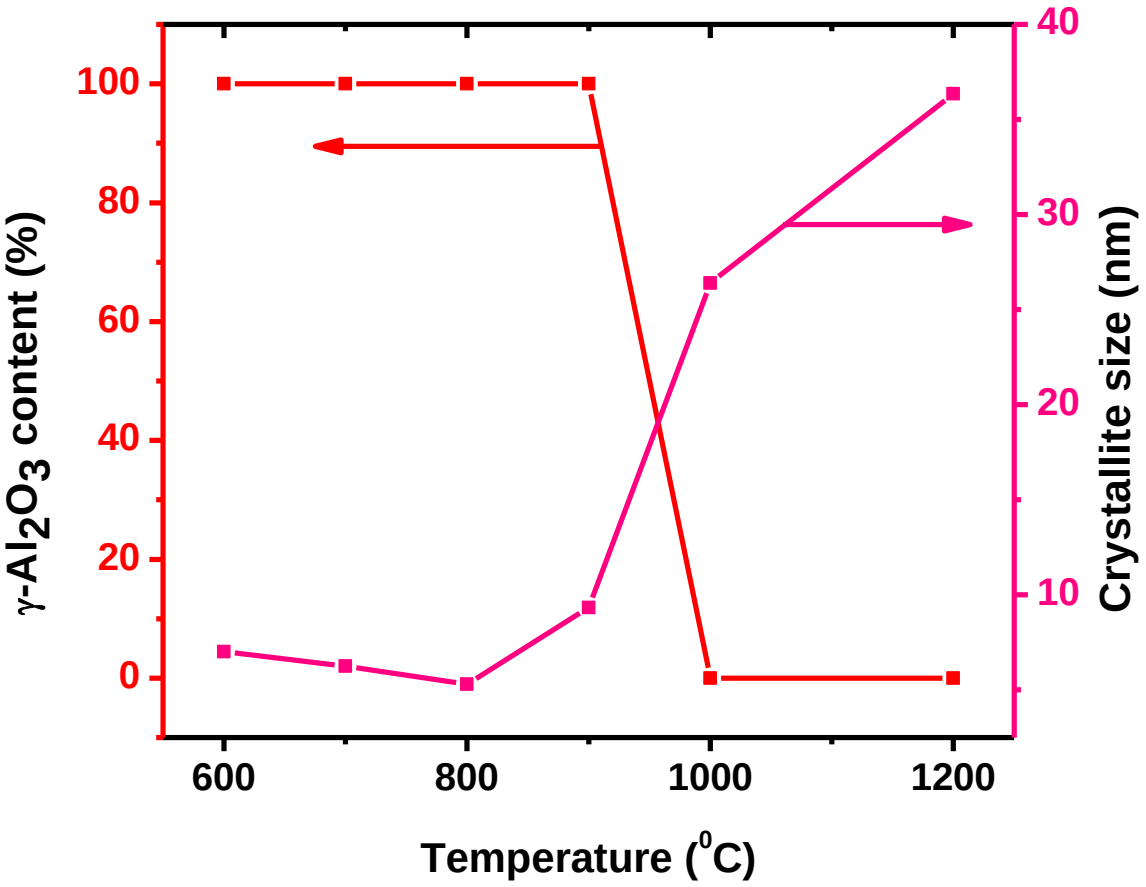

Fig. 4.2: Relationship between γ-Al_2O_3 to α-Al_2O_3 phase transition and the crystallite size obtained from XRD patterns.

4.1.3 Morphology of the Synthesized Material (FE-SEM and TEM)

The morphological structure and chemical composition of as-prepared nanocrystalline Al_2O_3 were studied using field emission scanning electron microscopy (FE-SEM) and energy dispersive X-ray spectroscopy (EDS) respectively as depicted in **Figure 4.3 (c)** and **(d)**. For comparison, the morphology and chemical composition of our parent material (Al metal powder) were also investigated via scanning electron microscopy (SEM) and EDS correspondingly as shown in **Figures 4.3 (a) and (b)**. From **Figure 4.3 (a),** it is evidenced that the morphology of Al metal powder- our starting material was non-spherical in shape with an average diameter of 70.474 μm. **Figure 4.3 (b)** depicts EDS spectrum of Al metal powder revealing its chemical composition of 99.1 % Al and 0.1 % Mg. **Figure 4.3 (c)** depicts FE-SEM image of the prepared alumina. It is crystal clear that the morphology of the prepared alumina nanoparticles is almost spherical in shape with an average diameter of 18.963 nm. **Figure 4.3 (d)** depicts the EDS spectrum of the selected 7 μm^2 on the surface of the prepared alumina. The existence of Aluminum and Oxygen in the EDS spectrum reveals the formation of Aluminum oxide which confirms our XPS results.

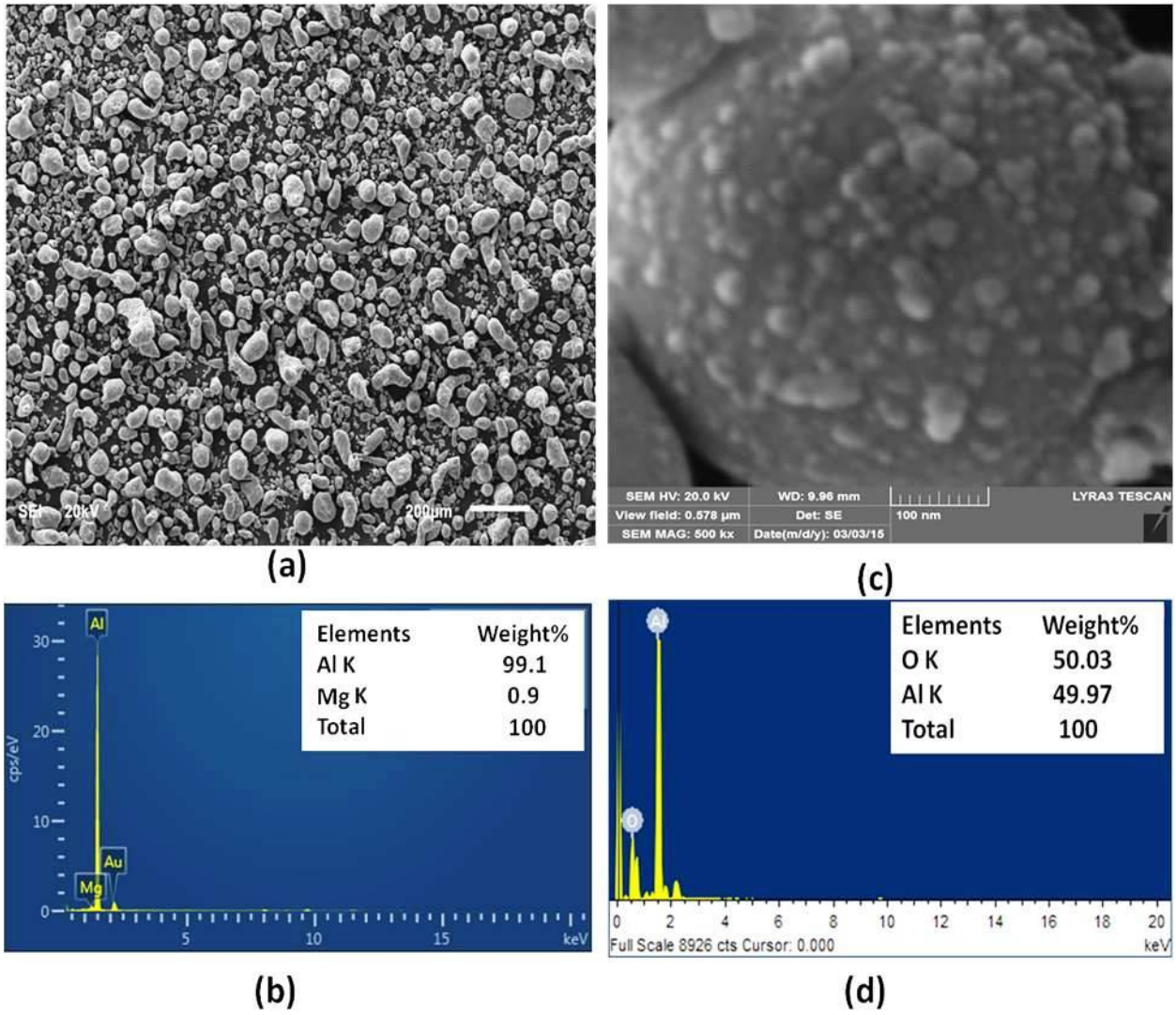

Fig. 4.3: (a) SEM micrograph of the parent material (Aluminium powder); (b) FE-SEM image of the prepared nanocrystalline Al_2O_3; (c) EDS spectrum of the parent material (Al material); (d) EDS spectrum of the prepared Al_2O_3.

The TEM micrograph of alumina annealed at 900^0C for γ-alumina is depicted in **Figure 4.4 (a)** with its selected area electron diffraction (SAED) depicted in **Figure 4.4 (b)**. The TEM micrograph indicates the nanocrystalline nature of our sample which is in close consensus with the crystalline size calculated from XRD using Scherrer formula. **Figures 4.4 (c)** and **(d)** depict the TEM image and SAED of α-alumina heated at 1000^0C for 2 hours respectively while **Figures 4.4 (e) and 4.4 (f)** depict the TEM image and SAED of α-alumina heated at 1200^0C for 2 hours as well. The transformation of all pure alumina into the single α phase was noted at the temperature of 1000^0C and above as indicated by **Figures 4.4 (c**) and **4.4 (e)** with the crystallinity increases as the temperature increases. This is evident from Figures **4.4 (b)**, **4.4 (d)** and **4.4 (f)** that depict the SAED of the alumina annealed at 900, 1000 and 1200^0C respectively. Amorphous samples show no distinguishable diffraction pattern. On the other hand, crystalline samples give a spot pattern that is peculiar to a particular crystal and the number of spot pattern corresponds to the degree of crystallinity of that sample. The spot pattern increases from **Figure 4.4 (b), (d) to (f)** which indicates that the crystallinity of our sample increases as the temperature increases. As a result of the annealing temperature, all these alumina nano powders vividly appear to be in agglomerated form.

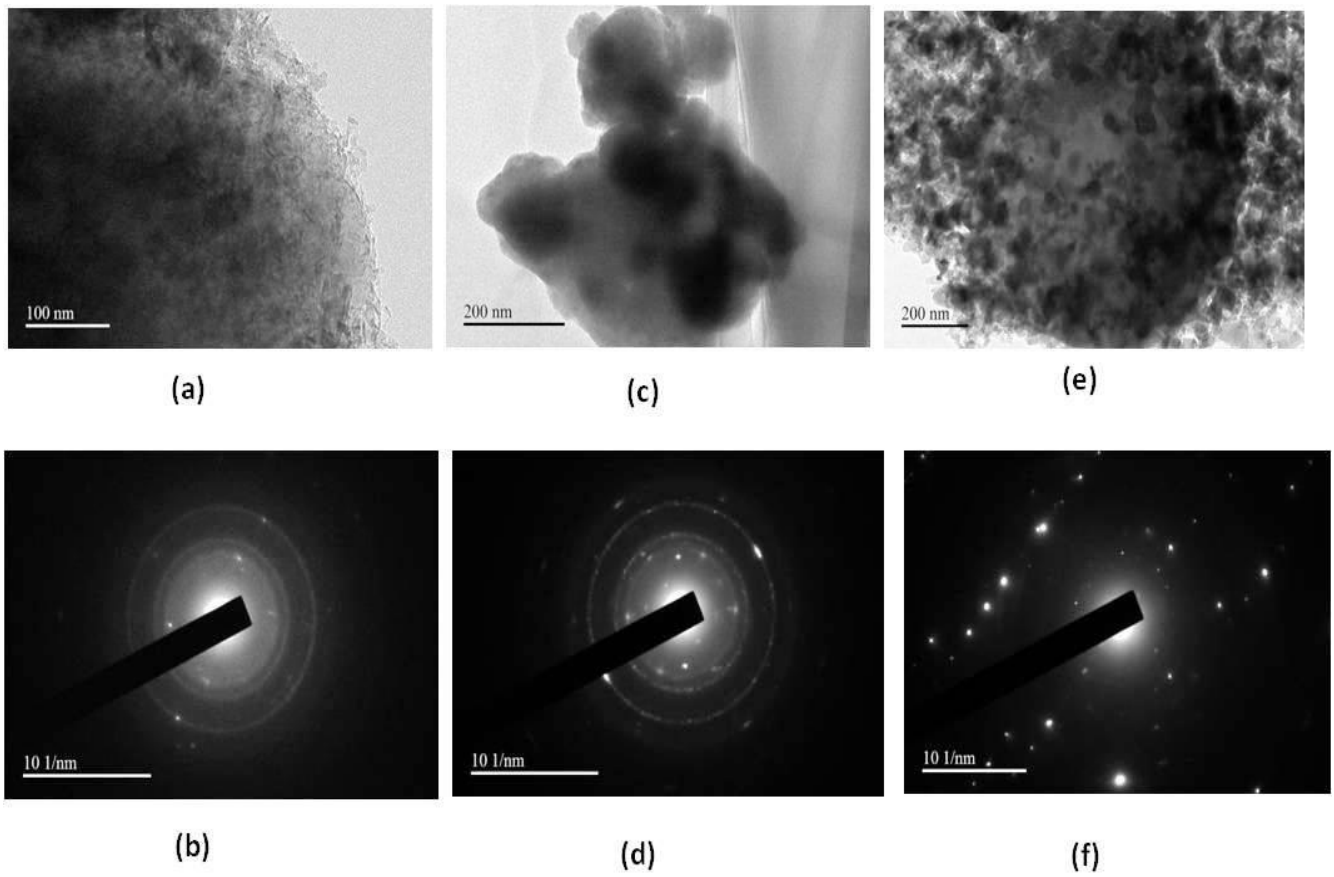

Fig. 4.4: (a) TEM micrograph of nanocrystalline Al_2O_3 annealed at 900^0C for 2 hrs; (b) SAED patterns micrograph of Al_2O_3 annealed at 900^0C for 2 hrs; (c) TEM micrograph of nanocrystalline Al_2O_3 annealed at 1000^0C for 2 hrs; (d) SAED patterns micrograph of Al_2O_3 annealed at `$1000^0$C for 2 hrs; (e) TEM micrograph of nanocrystalline $Al_2O_3$ annealed at $1200^0$C for 2 hrs; (f) SAED patterns micrograph of $Al_2O_3$ annealed at `1200^0C for 2 hrs.

4.1.4 Fourier Transform infrared Spectroscopy (FT-IR) study

The FTIR spectra of as-prepared Al_2O_3 nanopowder and Al_2O_3 nanopowder annealed at different temperature are depicted in **Figures 4.5 (a)-(g)**.

FTIR spectrum at 4000–400 cm^{-1} for the as prepared aluminum oxide nano-particles was conducted as depicted in **Figure 4.5 (a).** A sharp absorption bands in the wave number about 420 and 434 cm^{-1} reveal the formation of Al_2O_3 nanoparticles [116-117].

FTIR spectra of the Al_2O_3 nanoparticles products after annealing treatment were performed for a better comprehension of the structure of the nanoparticles. **Figures 4.5 (b)-(g)** depicts the FTIR spectra of the annealed samples at different temperatures, 600, 700, 800, 900, 1000 and 1200 ^oC. An absorption band revealing the vibrational properties of Al_2O_3 nanocrystals is observed in the range of 410– 495 cm^{-1}. This band is mainly assigned to the stretching vibrations of Al–O. This absorption band at about 434.7 cm^{-1} of the as prepared alumina. When the Al_2O_3 was annealed thermally, a shift of the IR absorption peak toward a low wave number (red shift) was observed and reaching 422.3 cm^{-1} when the temperature reached 700^oC and later increased to 450.7 cm^{-1} when the temperature reached 1200^oC, indicating the change in the alumina phase from crystallization phase γ-Al_2O_3 at 700^oC to α-Al_2O_3 crystallization phase at 1200^oC. There are also some wide and high peaks of AL–O stretching (AlO_4 or AlO_6 vibration) in the range of 400-1100 cm^{-1} that are related to the transitional phases of alumina and stable phase of α-Al_2O_3[118]. The other absorption peaks, like at the range between1450 to 1740 cm^{-1}, indicate some changes in the surface chemistry of alumina nanoparticles by environmental conditions such as absorption of CO_2 and moisture. The broad absorption

at 3500 cm^{-1} is characteristic stretching vibration of hydroxylates (O–H) resulted from the adsorption of moisture on the nanoparticles.

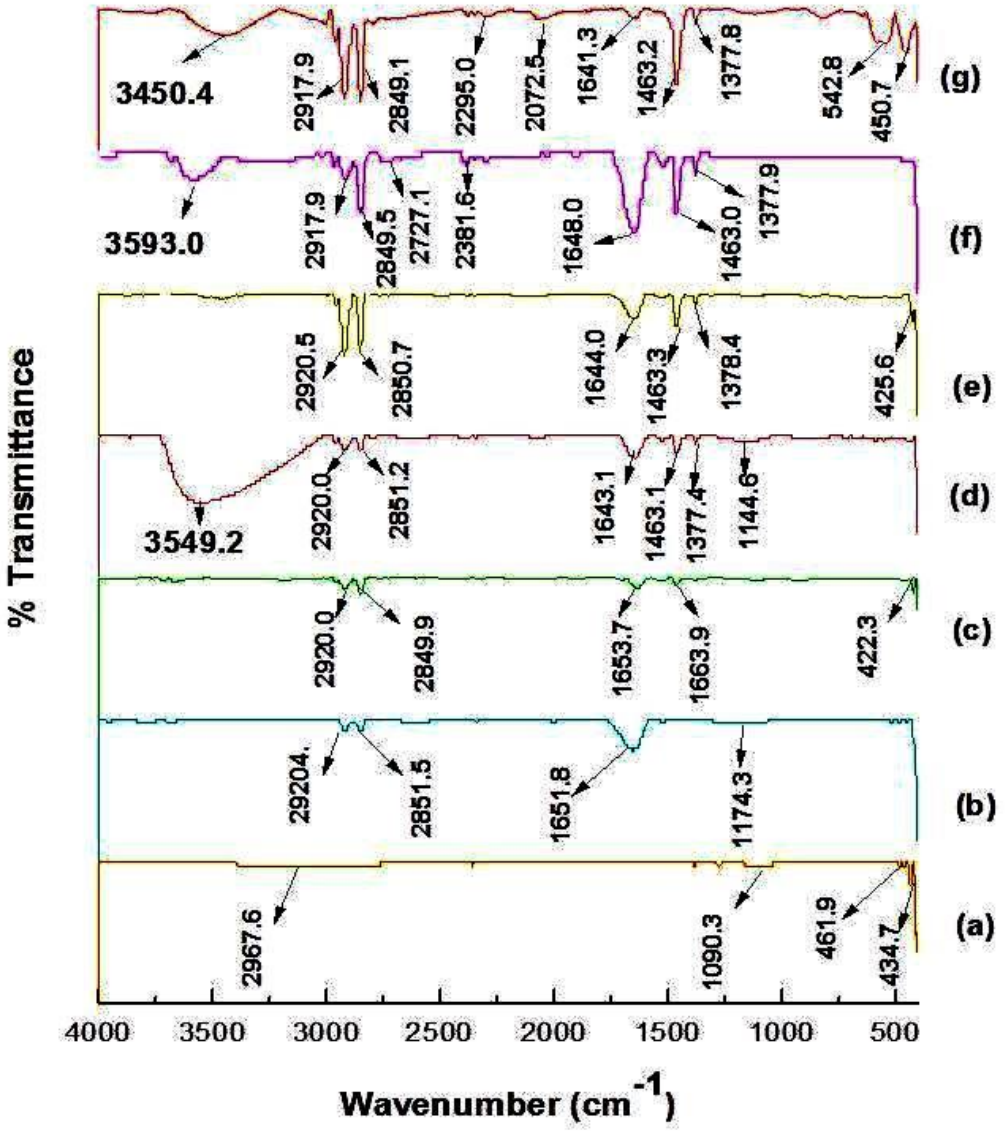

Figure 4.5: FT-IR of: (a) As- prepared Nano crystalline Al_2O_3 ; Nano crystalline Al_2O_3 annealed at (b) 600^0C ; (c) 700^0C (d) 800^0C (e) 900^0C (f) 1000^0C (g) 1200^0C for 2 hrs respectively.

4.1.5 XPS Analysis

Figure 4.6 depicts survey scans for the as prepared Al_2O_3 and the sample thermally treated at 700^0C. The elements present in each sample are clearly labeled in the figure. The samples contain Aluminum and oxygen only. The carbon present in the samples is due to air contamination. The sample treated at 1000 ^{0}C is not shown here, it has the same elements as the other two samples.

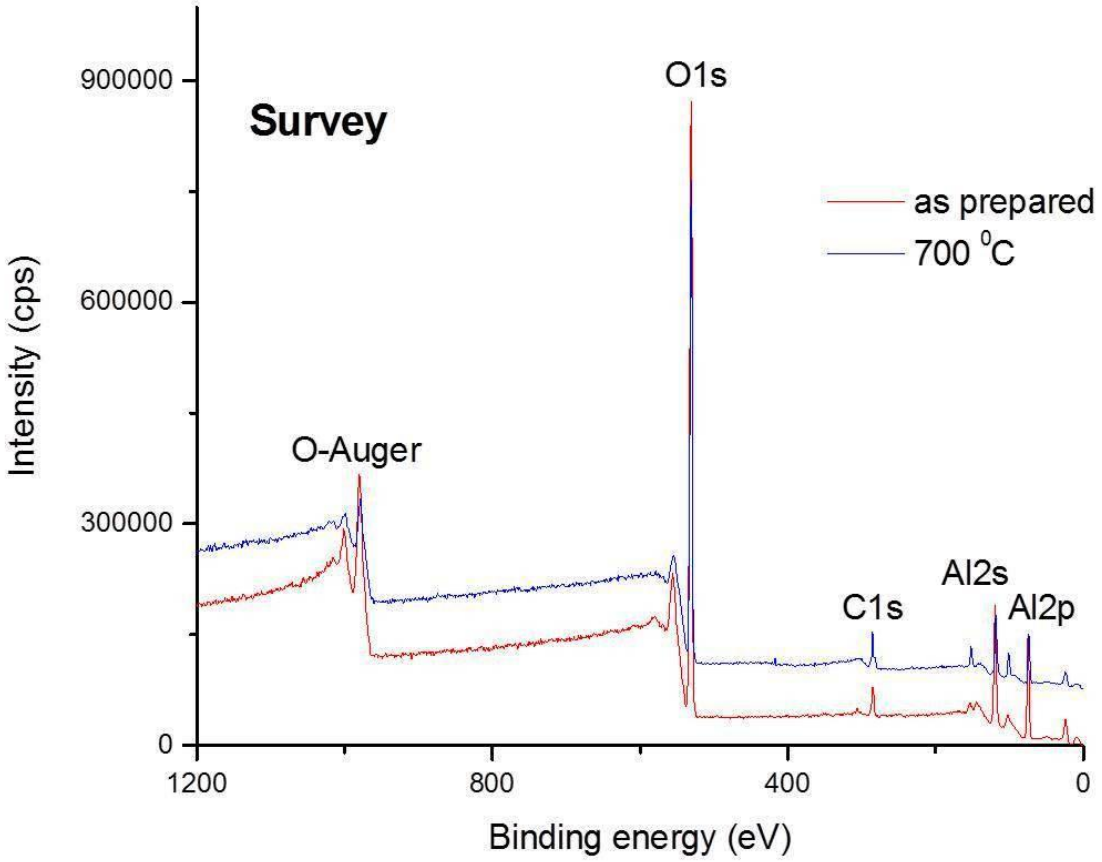

Figure 4.6: Survey scans for the as prepared and the sample heat treated at 700 ^{0}C. The elements present in each sample are clearly labeled in the spectra.

To determine the composition of the as-prepared and the heat treated samples, high resolution scans were collected for the Al 2p and O1s core level spectra. Figure 4.6 shows the fitted Al 2p core level spectrum from the as-prepared sample. A single peak was fitted to the experimental data with a binding energy of 74.8 eV and a full width at half maximum of 1.7 eV. These data agree with the literature [119]. The peaks for the heat treated samples are similar to the one shown in **Figure 4.7.**

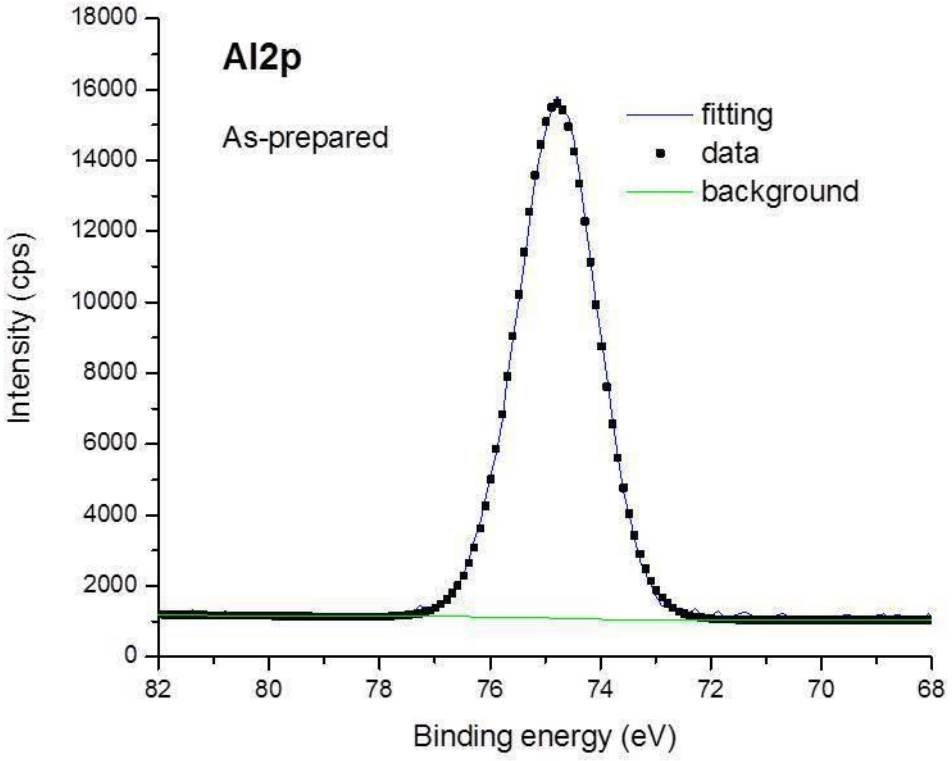

Figure 4.7: High resolution scan of Al 2p core level spectrum of the as-prepared sample.

The O1s spectrum of the as-prepared sample is shown in **Figure 4.8**. The peak has been fitted with a single contribution. The best fit to the data resulted in a binding energy of 530.9 eV and a full width at half maximum of 2.4 eV in good agreement with data from Thomas and Sherwood [120].

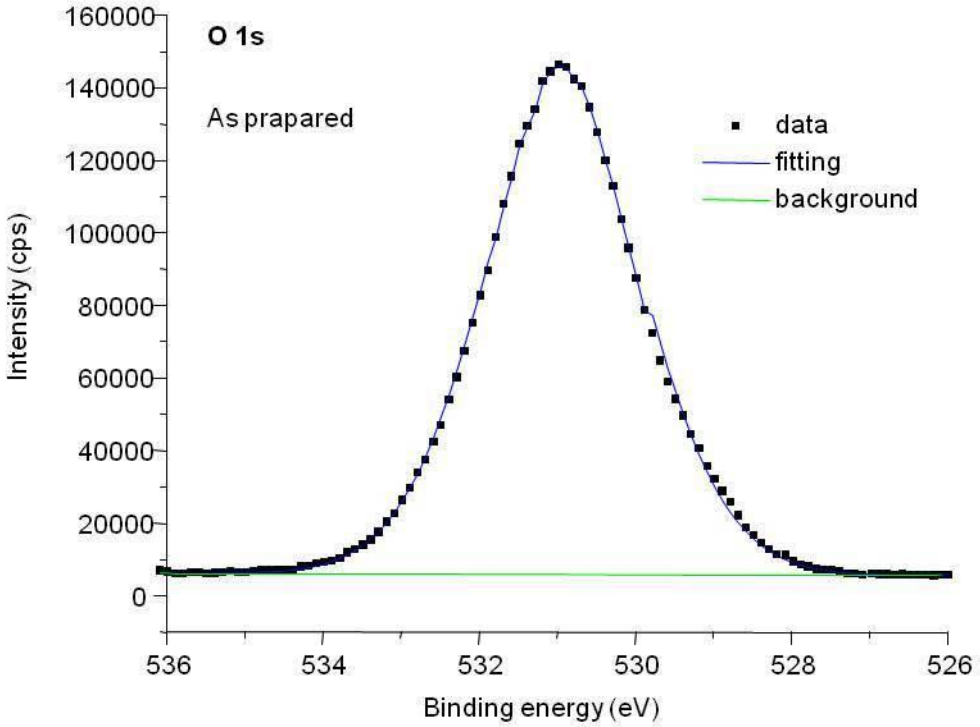

Figure 4.8: High resolution scan of O1s core level spectrum of the as-prepared sample.

Table 4.2 gives the detailed data from the fitting of the O1s and Al 2p spectra for the three samples investigated in this study. It is clear from the table that the stoichiometric compositions of the samples are very close to the desired nominal composition of Al_2O_3. The XPS data confirm that the formation of Al_2O_3 films was successfully accomplished in this study. The Al 2p XPS peaks for alumina in different phases have very close binding energies and therefore it is impossible to separate the peaks for each phase. The energy separation is about 0.3-0.4 eV on the average. See for example Handbook of X-ray Photoelectron Spectroscopy, appendix B [121].

Table 4.2: Data related to the fitting of the XPS spectra of Al 2p and O 1s. The error in the data is $\pm$ 10%.

Sample	O1s			Al2p		
	BE (eV)	FWHM (eV)	Wt%	BE (eV)	FWHM (eV)	Wt%
As prepared	530.9	2.4	65	74.8	1.7	35
700 ^{0}C	531.2	2.3	57	74.9	2.2	43
1000 ^{0}C	531.2	2.5	61	74.9	2.3	39

4.1.6 Thermo gravimetric Analysis (TGA and DSC)

Figure 4.9 shows the thermo gravimetric analysis (TGA) curve of the prepared alumina with three distinct weight loss steps with DSC curve indicating the significant change in the mass was around 200 °C. The first slow but gradual weight loss of about 15% is attributed to the removal of moisture and water molecules embedded inside the material.

The second dramatic loss of about 20% around 400°C is attributed to the phase transition. The third slow and gradual insignificant loss of 3% is attributed to another phase transition. At 550°C, the residual mass was found to be 65%.

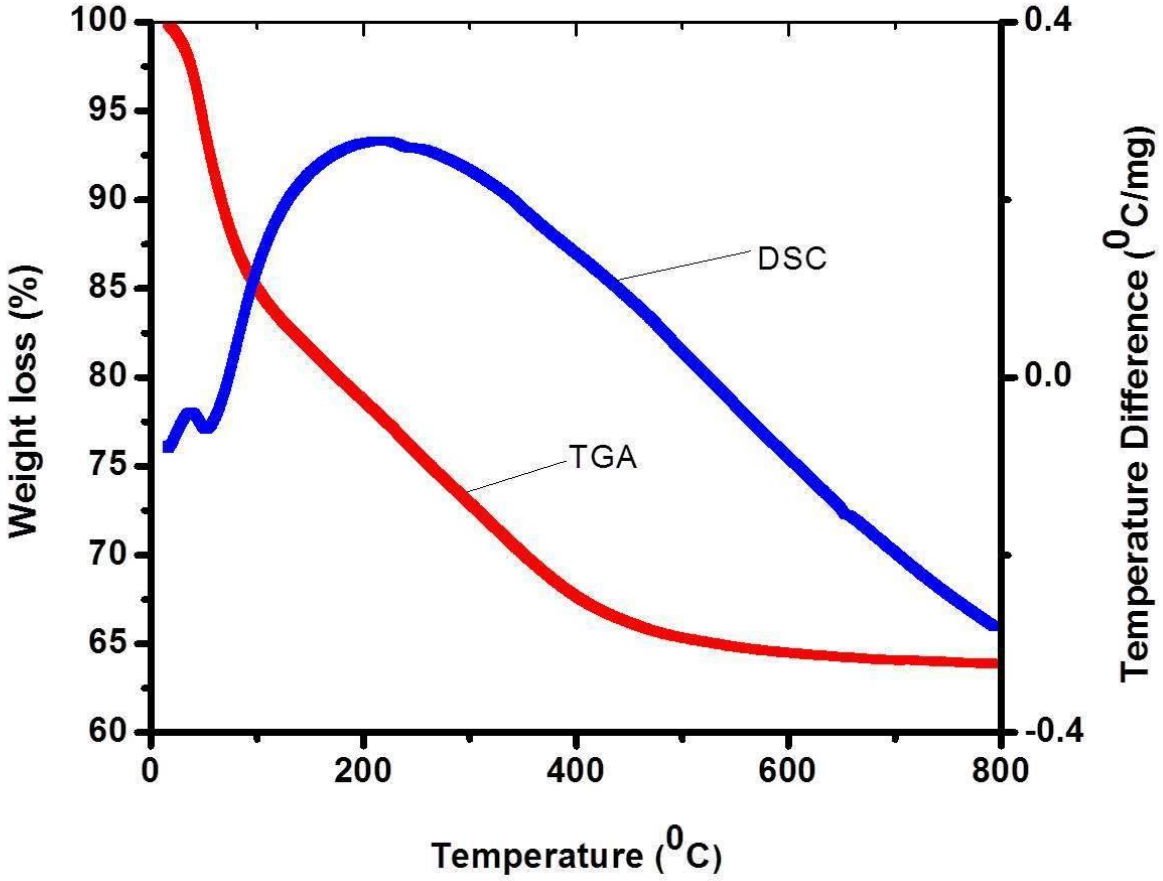

Figure 4.9: TGA/DTA analysis of the As-prepared nanocrystalline Al_2O_3 powders.

4.2 Synthesis and Characterization of Zirconium Oxide (ZrO_2) Nanoparticles (NPs)

In this section, the synthesis and characterization of colloidal zirconium oxide (ZrO_2) nanoparticles are elucidated. The effects of oxidizing media on the composition, morphology and optical features of the synthesized zirconia nanoparticles are discussed explicitly in the following subsections:

4.2.1 Synthesis of ZrO_2 Nano particles (NPs)

The experimental arrangement shown in **Fig. 3.1** was utilized for the production of ZrO_2 NPs. The micro-sized metallic Zirconium (Zr) powder was dispersed in about 15 ml of de-ionized water, ethanol and acetone accordingly. In each case, a high energy laser beam was used to irradiate the mixture. As a result of high intense laser irradiation, most of the laser beam was absorbed by the target (Zr metal powder) and lead to the break down in the sample and the plasma plume was ejected on the sample surface. The chemical reaction occurred during laser ablation between the ablated material (Zr metal powder) and the liquid environments and thus, produces a whitish colloid of ZrO_2 nanoparticles in de-ionized water, a whitish-dark colloid in ethanol and dark colloid in acetone respectively. **Fig. 4.10** depicts the colors and appearance of ZrO_2 nanoparticles produced in de-ionized water, ethanol and acetone respectively.

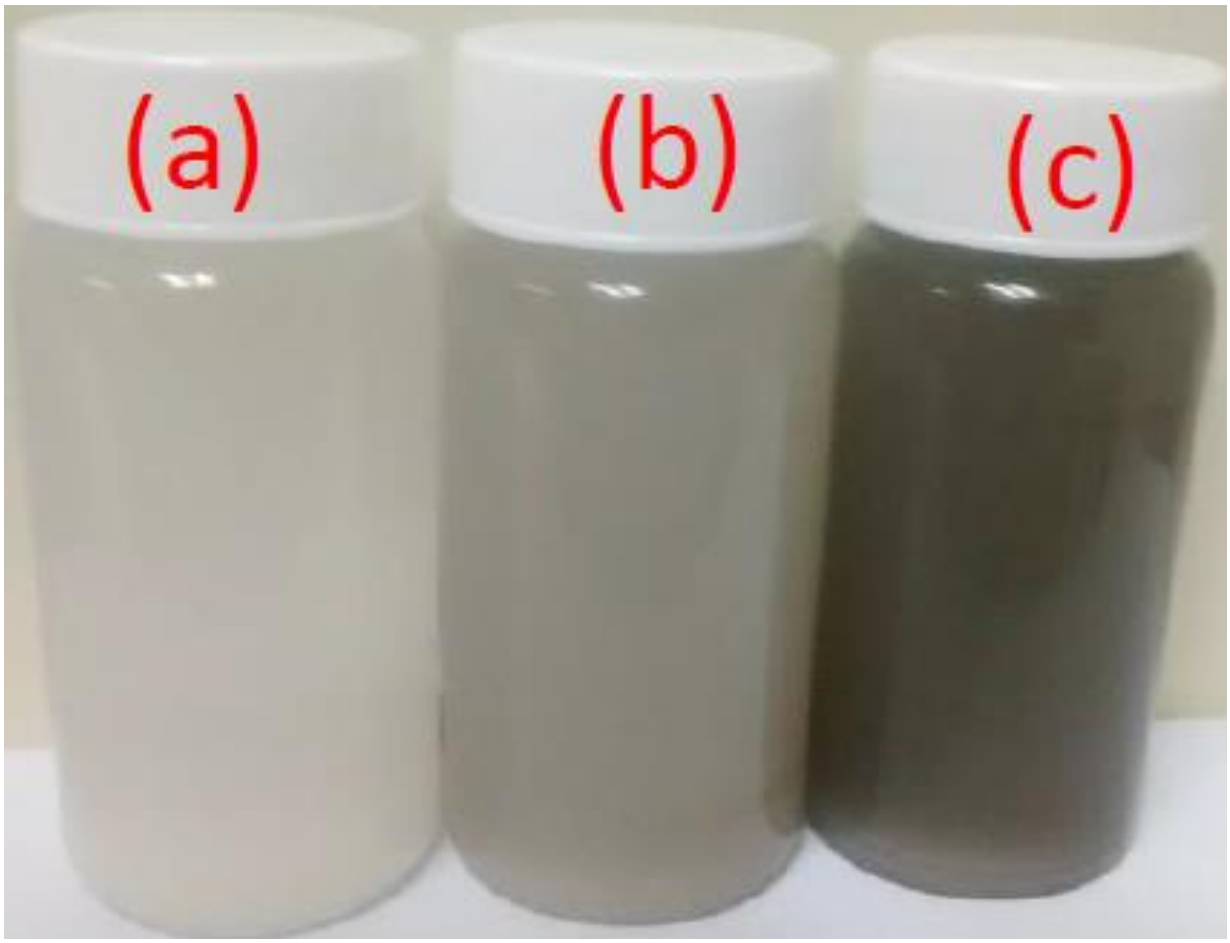

Fig. 4.10: The colour and appearance of colloidal ZrO_2 Nanoparticles synthsized using PLA in (a) Water (b) Ethanol and (c) Acetone.

The difference in colors of the nanoparticles produced was as a consequence of nuclei formation and the development of nano particles over the formed nuclei in different liquid environments. The different chemical and physical interactions of molten Zr metal with different liquid environments can also be responsible for the difference in their colors [96]. The obtained colloids of ZrO_2 nano particles in the three oxidizing media were collected and heated at a temperature of 50^0C for 3 hours to obtained nano powder ZrO_2 for the characterizations.

4.2.2 Structural Characterization of the synthesized ZrO_2 in different oxidizing media

X-ray diffraction (XRD) analysis was performed on the synthesized zirconia nanoparticles to study the crystalline structure of ZrO_2 in the three oxidizing media. Diffraction peaks at a specific angle and intensity reflects the information about a particular crystal like our finger print. **Fig. 4.11 (a), (b)** and **(c)** represent the X-ray diffraction patterns of the sample produced in water, ethanol and acetone respectively. Diffraction peaks in **figure 4.11 (a)** with 2θ values of 24.71, 28.40, 31.67, 42.21, 56.85, and 61.19 originate from the crystal planes (011) , (-111), (111), (12-1), (-113) and (113) of monoclinic phase of ZrO_2 respectively [JCPDS Nos. 00-037-1484, 00-088-2390] while diffraction peaks with 2θ values of 34.90, 35.34, 50.36 and 51.52 can be assigned to the crystal planes (002), (110), (112) and (200) of tetragonal phase of ZrO_2 accordingly[JCPDS No. 00-50-1089].

Diffraction peaks in **figure 4.11 (b)** with the 2θ values of 24.71, 28.40, 41.62, 49.49, 55.63, 57.31, 61.19 and 65.83 correspond to the crystal planes (011), (-111), (12-1), (21-

2), (221), (310) and (113) of monoclinic zirconia respectively[JCPDS No. 00-037-1484 and 01-088-2390] and those peaks at 35.24, 50.35 and 50.98 originate from (110), (112) and (020) crystal planes of tetragonal phase of zirconia respectively[01-079-1769]. In figure 4.10 c, the diffraction peaks at angles 2θ of 24.71, 28.40, 41.62, and 65.83 correspond to (011), (-111), (12-1) and (230) planes of monoclinic zirconia while peaks at 30.29 and 35.04 correspond to the crystal planes (101) and (110) of tetragonal zirconia accordingly.

From the information derived from X-ray diffraction patterns of the three samples, it is clear that the zirconium oxide nanoparticles produced via pulsed laser ablation in each of the oxidizing media (de-ionized water, ethanol and acetone) is a mixture of tetragonal and monoclinic phases. Similar result has been reported in the literature for the synthesis of zirconia via pulsed laser ablation in water [69, 122]. However, there was existence of Zr metal in the samples produced in ethanol and acetone as evidence from figure 4.10 b and c with the diffraction peaks at angles 2θ of 31.67, 51.39 and 56.43 corresponding to the crystal planes (100), (200) and (110) of hexagonal zirconium metal respectively[JCPDS Nos. 00-005-0665, 01-071-3958 and 01-089-3045]. The presence of this Zr metal is more in acetone than ethanol and there exists none in the sample produced in de-ionized water. This confirms that pure ZrO_2 nanoparticles are better produced via PLA in de-ionized water than ethanol and acetone.

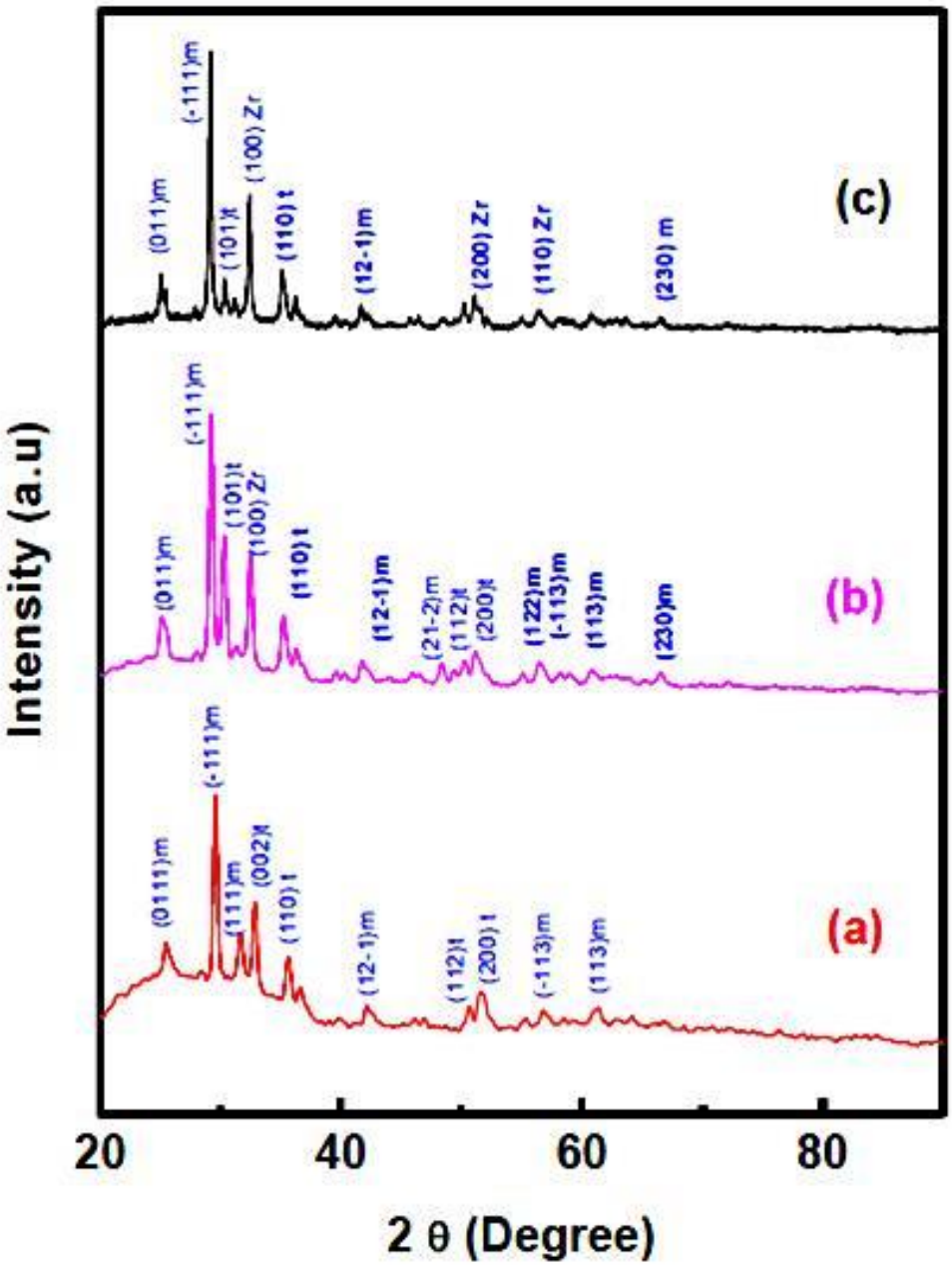

Fig. 4.11: X-ray diffraction patterns of ZrO_2 nanoparticles synthesized via pulsed laser ablation in (a) Water (b) Ethanol (c) Acetone. t, m represent tetragonal and monoclinic phases of zirconia respectively.

The crystallite size of ZrO_2 NPs was estimated using Scherrer's formula. The average crystallite sizes calculated were found to be 41.8 nm, 42.6 nm and 40.3 nm in water, ethanol and acetone for the monoclinic phase of ZrO_2 while 20.1 nm, 24.8 nm and 18.9 nm were obtained as the average crystallite of tetragonal phase of ZrO_2 NPs prepared in water, ethanol and acetone accordingly. This finding is also in agreement with the data published earlier [123]. According to Garvie, the presence of tetragonal phase is due to the critical size effect and proved experimentally the existence of a critically size of ~ 30 nm below which the metastable tetragonal phase is stable and above which the monoclinic phase is stable[123].

4.2.3 Morphological Studies

The morphology of zirconium metal powder used as our precursor was investigated with the aid a JEOL JSM-6610LV scanning electron microscope. To confirm the morphology of ZrO_2 nanoparticles produced in this study, we emploed JEM-2100F TEM machine manufactured by JEOL, USA. **Fig. 4.12 (a)** indicating SEM image of zirconium (Zr) metal powder confirms that our starting material is in microscale. **Fig. 4.11 (b, c, d)** represent the TEM image of ZrO_2 fabricated via PLA in water, ethanol and acetone respectivly. The TEM images confirmed that the particles in each of the three sample are almost spherical in shape with particles sizes ranges between ~10 nm to 50 nm with smaller particles less than 10 nm

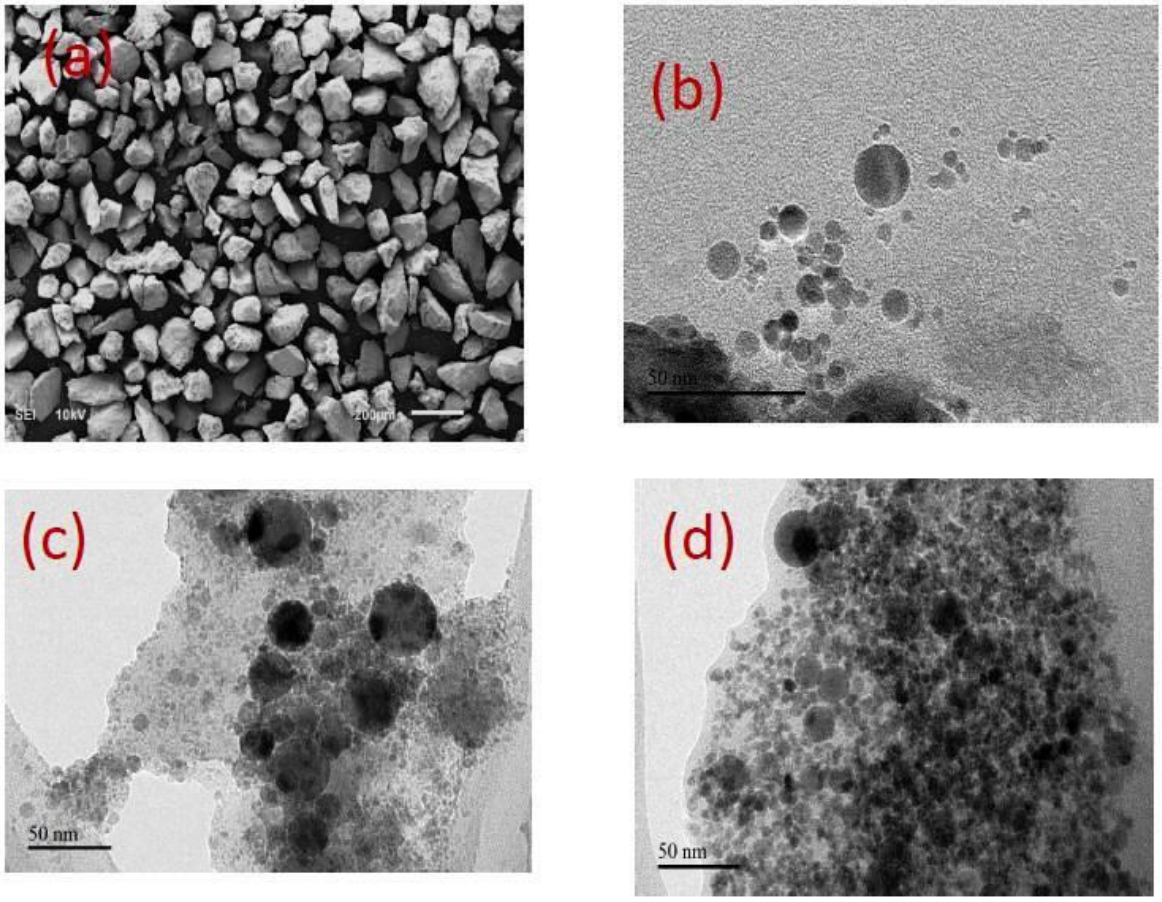

Fig. 4.12: (a) SEM micrograph of Zirconium metal powder employed as our precursor. TEM micrographs of ZrO2 synthesized via PLA in (b) Water (c) Ethanol and (d) Acetone respectively.

4.2.4 Uv-Vis Absorption Spectroscopy Study

Uv-Vis spectroscopy works on the basis of Beer's law as given in **equation 4.1**

$$\boldsymbol{A = \log(\frac{I_0}{I}) = \varepsilon bc} \qquad \textbf{4.1}$$

Where A stands for absorbance, $\boldsymbol{I_0}$ is a measure of the incident radiation intensity while the transmitted intensity is denoted by $\boldsymbol{I}$. The molar absorptivity is $\boldsymbol{\varepsilon}$, **b** is the path length and **c** is the sample concentration. In this study, the path length b is fixed with the aid of using the same quartz cuvette for the three samples. To investigate the effect of liquid media on the ZrO_2 nanoparticles synthesized via pulsed laser ablation in liquids, absorption spectra of the colloidal ZrO_2 nanoparticles produced in water, ethanol and acetone were recorded in the region 200-800 nm wavelength. **Fig. 4.13 (a, a, c)** present the optical absorption spectra of ZrO_2 nanoparticles produced in the three oxidizing media to ascertain the formation efficiency of ZrO_2 nanoparticles in these liquid media. The characteristics absorption of colloidal nanoparticles is due to the proper surface plasmon resonance which is determined by the nature of the materials, nanoparticle's size and concentration. The nanoparticle solution from de-ionized water had a higher absorption than either of ethanol and acetone as evidenced from **Fig. 4.13 (a,b,c).** The higher absorption is attributed to a higher nanoparticles concentration. Thus, water is a better medium of ablation to produce zirconia nanoparticles compared to ethanol and acetone. The Uv-Vis absorption by colloid of nanoparticles from de-ionized water and acetone had a maximum absorption at 208 nm as a result of inter-band transition of Zirconium electrons close to Fermi levels [124-125]. The absorption peaks at 250.9 nm and 323 nm in colloid of NPs from acetone, 237.5 nm and 278 nm in colloids of NPs

from ethanol and 238.9 nm in colloid of NPs from De-ionized indicate the formation of non-uniform sizes and a particle coagulation shift in wavelength of maximum optical extinction [126]. With all three liquids, there was a continuous absorption throughout the visible wavelength region that extends up to 1100 nm. These findings agreed with Mie theory. According to Mie theory, the ultraviolet and visible absorption behavior for 10 nm zirconium nanoparticles indicates a maximum absorption at 200 nm and a broad absorption peak at 300 nm that decays into a continuous small absorption [127].

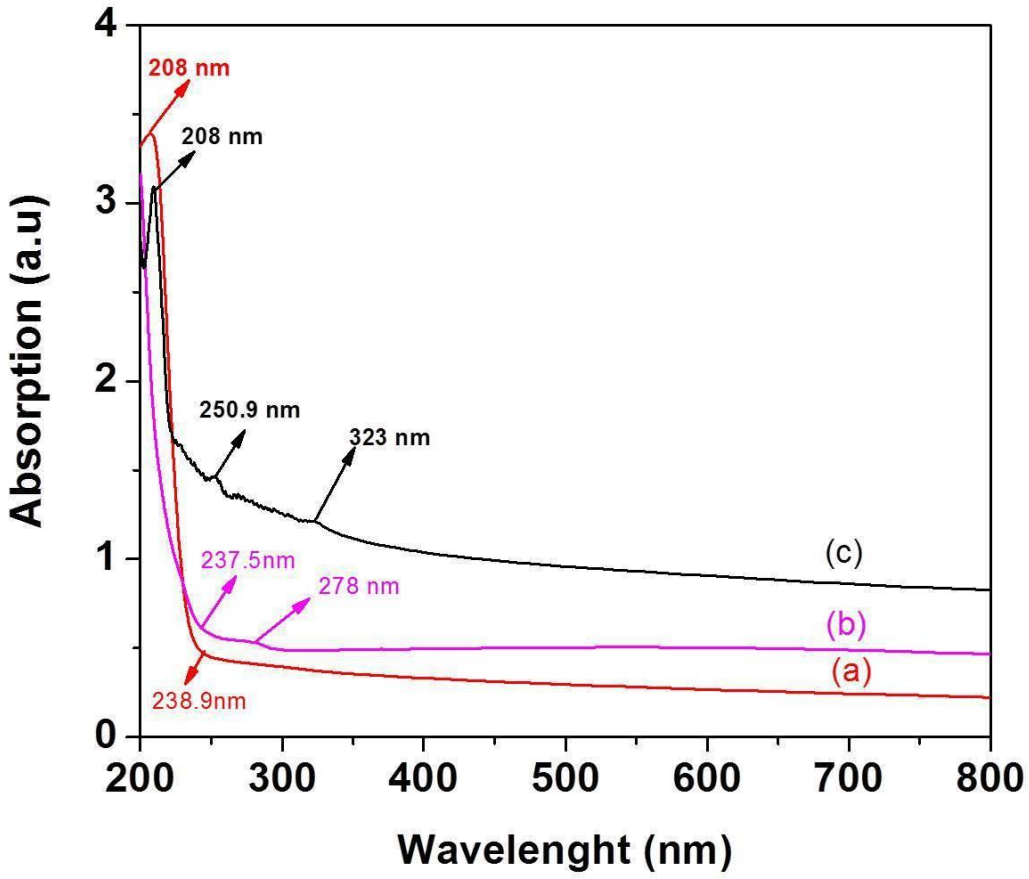

Fig. 4.13: Uv-Vis absorption spectra of ZrO2 nanoparticles synthesized via pulsed laser ablation (532 nm) in (a) Water (b) Ethanol and (c) Acetone respectively.

4.2.4.1 Band Gap measurement

Decreasing the size of nanomaterilas can cause significant change in the optical band gap of metal oxides by reduction of the valence and conduction bands[89]. Other factors like defect centers, mechanical stress and degree of crystallinity could also affect the optical band gap of metal oxides. From the Tauc plot shown in **Fig. 4.14 (a,b,c),** the band gap of colloidal suspension of ZrO_2 prepared in three different liquids was determined. For a direct band gap material such as zirconia, the absorption coefficient $\alpha(v)$ is directly proportional to $(E-E_g)^{½}$ where E represents the photon energy and E_g stands for the band gap energy. By extrpolating the linear part from higher absorption region of the plot $(\alpha hv)^2$ against hv to photon energy axis for zero absorption coefficient, we obatined the band gap (**Fig. 4.14**) to be 5.19 eV, 5.22 eV and 4.94 eV in water, ethanol and acetone respectively. In the lietrature, the band gap of ZrO_2 was reported in the range 5 – 5.5 eV[69], a slight variation reported in the band gap of ZrO_2 prepared in acetone could be atrributed to the presence of zirconia phase, defect state and morpholgy.

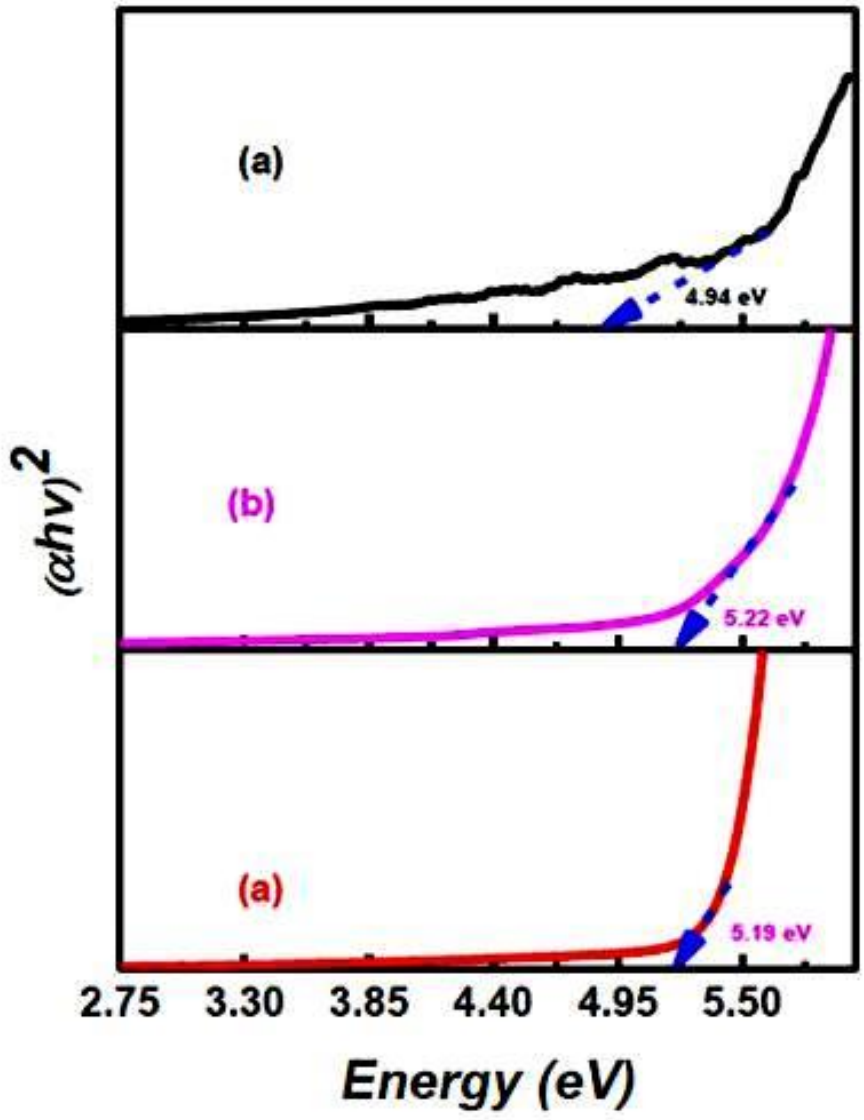

Fig. 4.14: Tauc plot of $(\alpha hv)^2$ versus hv for ZrO2 synthesized in (a) Water (b) Ethanol and (c) Acetone to evaluate the band gap ZrO_2 in each of the liquid environments.

4.2.5 Fourier Transform Infrared Analysis

Figure 4.15 depicts the FT-IR spectra of the ZrO_2 samples applied to confirm the molecular nature and the presence of the functional groups adsorbed on the nanostructured ZrO_2 synthesized via pulsed laser ablation in different liquids media. In **figure 4.15 a - c**, it can be noticed that the samples exhibited absorption peaks situated in the region 400-800 cm^{-1} which shows Zr-O stretching bond and therefore confirms the formation of ZrO_2 nanoparticles in the three samples [128-129]. The absorption broad bands observed in the region 3000-3600 cm^{-1} and some well-defined bands between 1300-1750 cm^{-1} correspond to the vibration of modes of O-H bond as a result of the adsorbed water molecules or hydroxyl groups on the surface of the synthesized ZrO_2 nanoparticles [130-132]. Theses absorption peaks around 3000-3600 cm^{-1} can also be assigned to the hydroxyl group of moisture, alcohol and acetone. The band exhibited around 1000 cm^{-1} in **figure 4.15 (a)** is a characteristic of peroxide (O-O) groups [128-129]. In figure 4.14 b and c, the absorption peaks at 1180 cm^{-1} could be assigned to C-O stretch or C-C bonds from ethanol and acetone respectively. The absorption peaks at 2810 cm^{-1} and 2910 cm^{-1} in figure 4.14 b and c respectively could be ascribed to the occurrence of C-H bond.

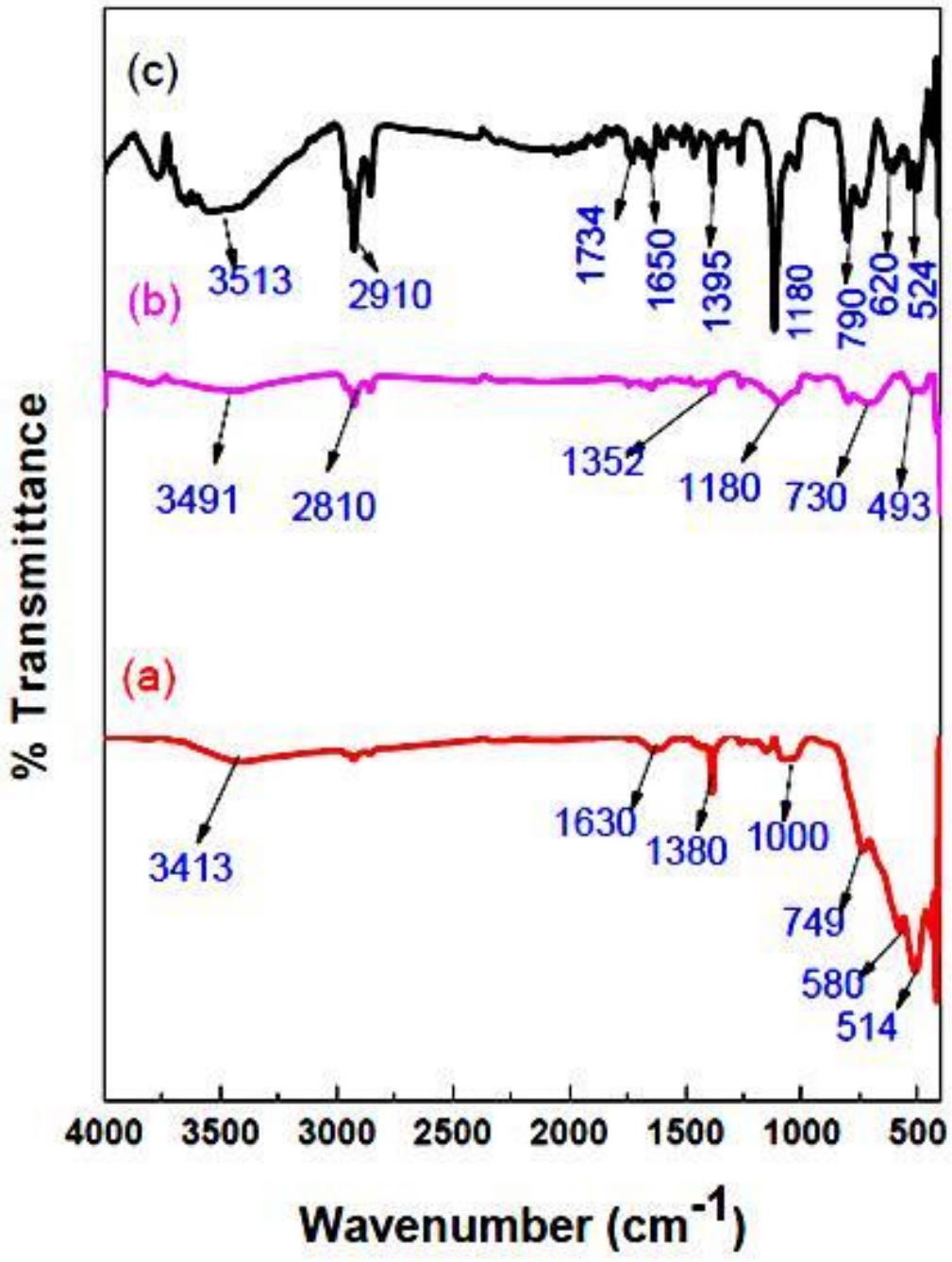

Fig. 4.15: FTIR spectra of ZrO2 nanoparticles synthesized via pulsed laser ablation in (a) water (b) Ethanol and (c) Acetone.

4.2.6 X-ray photoelectron Spectroscopy (XPS) study

The survey scans of ZrO_2 nanoparticles synthesized using pulsed laser ablation in water, ethanol and acetone are shown in **Fig. 4.16 (a, b, c)** respectively. The elements present in each sample were clearly identified. The samples contain the elements Zirconium, Oxygen, and Carbon. The carbon present in the sample prepared in water is from air contamination and was removed by Ar^+ bombardment. Its binding energy (BE) is at 284.6 eV.

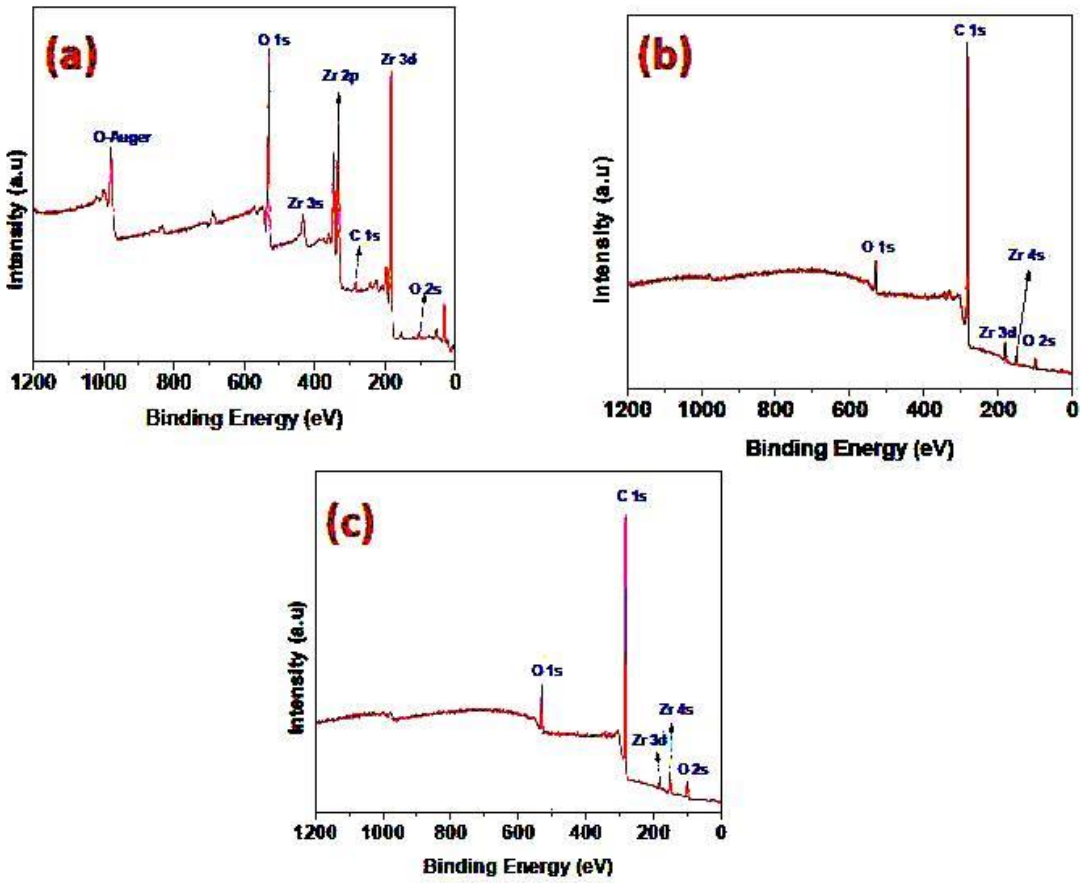

Figure 4.16: Survey scans of ZrO_2 nanoparticles synthesized in: (a) Water (b) Ethanol and (c) Acetone. Peaks from the elements present in the samples are clearly labeled.

In order to confirm the composition of the three samples, high resolution scans were recorded for Zr 3d, O 1s and C 1s core level spectra. **Fig. 4.17 (a, b, c)** represent the fitted spectra of Zr 3d spin-orbit doublet peaks of the three samples. Fig. 4.16 a shows Zr 3d spin-orbit doublets fitted with two contributions, one from nanocrystalline ZrO_2 and the other from Zr(OH). The Zr 3d doublet peaks from ZrO_2 has BE 181.9 eV and 184.3 eV with an energy separation of **2.4 eV, corresponding to contributions from Zr 3d5/2 and Zr 3d3/2,** respectively. The full width at half maximum (FWHM) is 1.7 eV for both peaks. The Zr 3d doublet peaks from Zr(OH) has BE 182.9 eV and 185.3 eV with an energy separation of 2.4 eV, corresponding to contributions from Zr 3d5/2 and Zr 3d3/2, respectively. The full width at half maximum (FWHM) is 1.9 eV for both peaks. This finding is in good agreement with literature [133-134]. The atomic percent found from the fittings of Zr 3d and O 1s spectra for Zr and O were calculated to be 34.1% and 65.9%, respectively. This is very close to stoichiometric composition of ZrO_2 compound. It is to be noted that the contribution of Zr(OH) was not included in the calculation of the atomic percent as it does not contribute to ZrO_2.

Also, doublet peaks were observed in the samples produced in ethanol and acetone corresponding to Zr $3d_{5/2}$ and Zr $3d_{3/2}$ at BE 180.9 eV and 183.3 eV, with an energy separation of 2.4 eV**.** The full width at half maximum (FWHM) is 1.8 eV for both samples. The fitting parameters for Zr 3d spectra of the three samples are reported in **Table 4.3**. The atomic % in this case was calculated to be 1.0% for Zr, 4.4% for O, and 94.6% for C for ethanol. The atomic % in this case was calculated to be 0.6% for Zr, 6.2% for O, and 93.2% for C for acetone. It is clear from these data, that the samples contain mainly C. The amount of Zr is too small. This can also be checked from the

survey scans where the C 1s peaks are predominant and the others are very small. We can conclude that the synthesis of ZrO_2 compound is better accomplished in de-ionized water.

Table4.3: Peak positions and FWHM from the fittings of the Zr3d from ZrO_2 nanoparticles synthesized in water, ethanol, and acetone.

Sample	**Zr $3d_{5/2}$ (ZrO2) B.E FWHM (eV)**	**Zr $3d_{3/2}$ (ZrO2) B.E FWHM(eV)**	**Zr $3d_{5/2}$ (Zr(OH)) B.E FWHM (eV)**	**Zr $3d_{3/2}$ (Zr(OH)) B.E FWHM(eV)**
Water	181.9 1.7	184.3 1.7	182.9 1.8	185.3 1.8
Ethanol	180.9 1.7	183.3 1.7	-	-
Acetone	180.9 1.8	183.3 1.8	-	-

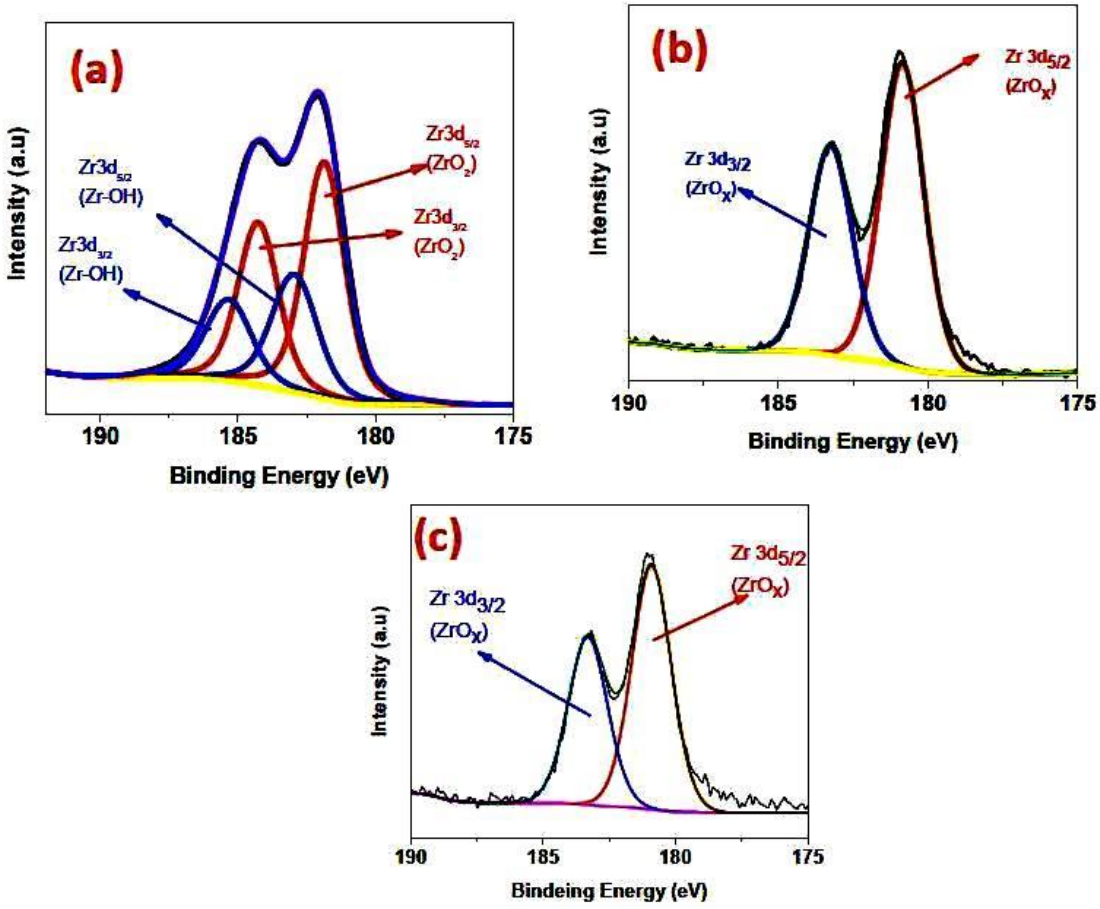

Fig.4.17: XPS spectra of Zr3d spin-orbit doublet peaks of ZrO2 nanoparticles synthesized in: (a) water (b) Ethanol (c) Acetone. The peaks are fitted with two contributions, one from ZrO2 and the other from Zr(OH).

Fig. 4.18 (a, b, c) shows the spectra of O 1s peaks of ZrO_2 nanoparticles produced in water, ethanol and acetone respectively. **Fig. 4.18 (a)** shows O 1s spectrum in water. The peak is fitted with three contributions; zirconium oxide (Zr-O), zirconium hydroxide (Zr-OH) and silicon dioxide (Si-O). The O 1s peak of silicon dioxide (SiO_2) is located around 534.1 eV with full width at half maximum of 3.3 eV, zirconium hydroxide is found at 531.4 eV, FWHM of 2.6 eV and nanocrystalline ZrO_2 is centered at 529.7 eV with FWHM of 1.9 eV. This is in a very good agreement with the literature [135]. **Fig. 4.18 (b,c)** represent O 1s spectra of ZrO_x produced in ethanol and acetone respectively. In both samples, the spectra were fitted from only two contributions one from oxygen bonded to Si (Si-O) and the other from oxygen bonded to Zr (Zr-O_x). For the sample prepared in ethanol, the first O 1s fitted peak is centered at 530.3 eV with FWHM of 3.0 eV, while the second fitted peak is centered at a binding energy of 533.7 eV with FWHM of 2.6 eV. The results from O 1s spectra satisfactorily confirmed the formation of ZrOx [138]. However, the FWHM value obtained is large (3.0 eV) means that the whole peak assigned to Zr-O_x at 530.3 eV cannot be assigned to Zr-O_x alone. It could be due to a contribution from C-O bonding at a reported BE of 530.5 eV [138]. The detailed data from the fittings of the O 1s spectra for the three samples are presented in **Table 4.4.**

Table4.4: Peak positions and FWHM from the fittings of the O1s from ZrO_2 nanoparticles synthesized in water, ethanol, and acetone.

Sample	**O 1s (Zr-O)** **B.E/FwHM (eV)**	**O 1s (Zr-OH)** **B.E/FWHM (eV)**	**O 1s (Si-O)** **B.E/ FWHM(eV)**
Water	529.7 1.9	531.4 3.3	534.1 2.3
Ethanol	530.3 3.0	_	533.7 2.6
Acetone	530.5 2.6	_	533.3 2.6

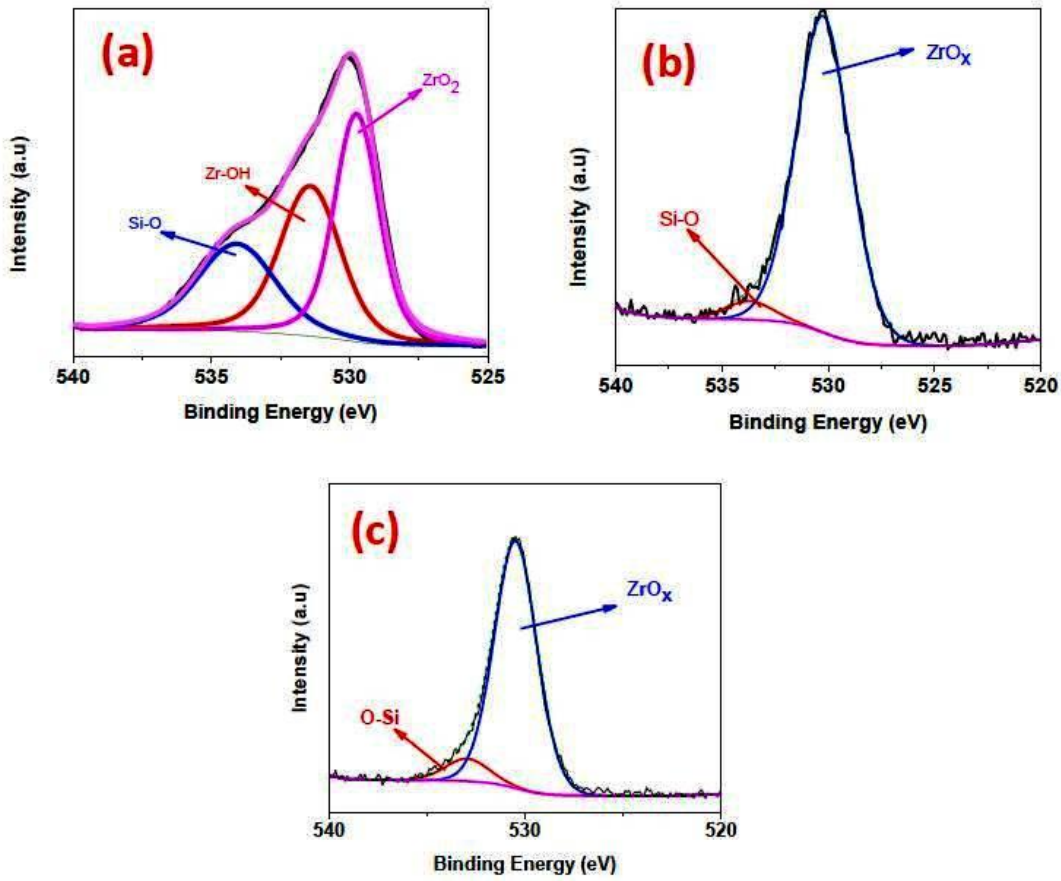

Fig.4.18: XPS spectra of O1s peak of ZrO2 nanoparticles synthesized in (a) water (b) Ethanol and (c) Acetone. The spectrum is fitted with three contributions: ZrO2, Zr(OH) and Si-O.

Fig. 4.19 (a,b) show XPS spectra of C1s peak of ZrO_2 nanoparticles synthesized in ethanol and acetone. The spectra peaks were fitted with one contribution from Zr-C with the binding energy located around 282.8 eV and FWHM of 1.8 eV for ZrO_x synthesized in both ethanol and acetone. Zirconium carbide (Zr-C) formed could be as a result Ar^+ ion bombardment used to remove surface impurities from the samples [137]. The fitting parameters of the C 1s spectra for the two samples are presented in **Table 4.5**. From the analysis of the experimental results obtained from XPS, it can be concluded that de-ionized water is a better oxidizing medium to synthesize stoichiometric zirconia nanoparticles than ethanol and acetone.

Table4.5: Peak positions and FWHM from the fittings of the C1s from ZrO2 nanoparticles synthesized in ethanol, and acetone.

Sample	**C 1s Zr-C** **B.E** **FWHM (eV)**
Ethanol	282.9 1.8
Acetone	282.8 1.8

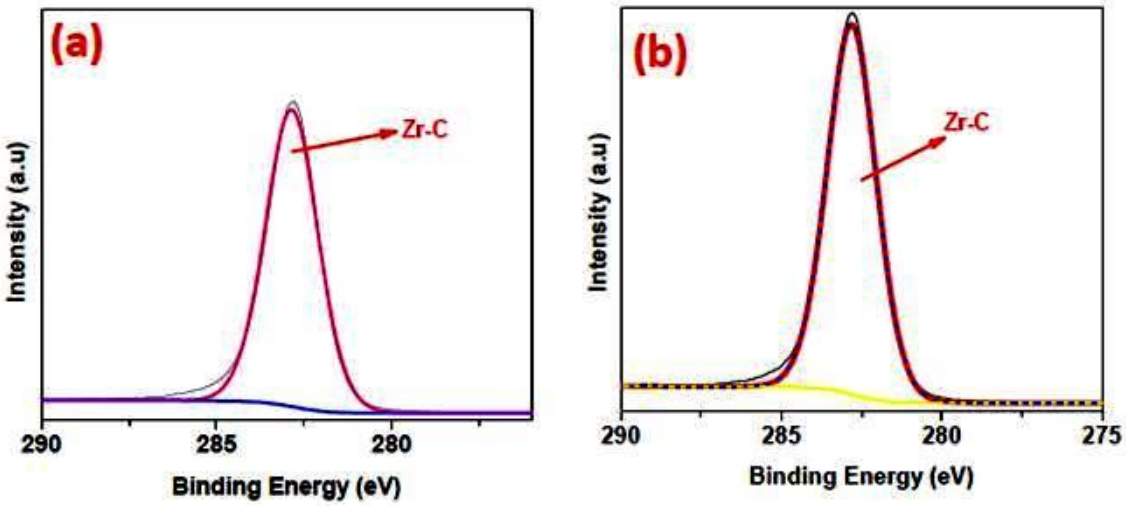

Fig.4.19: XPS spectra of C1s peak of ZrO2 nanoparticles synthesized in (a) Ethanol and (c) Acetone. The peak is fitted with one contribution from Zr-C.

CHAPTER 5

CONCLUSION AND RECOMMENDATIONS

5.1 CONCLUSION

Metal Oxides (Al_2O_3 and ZrO_2) were successfully synthesized from the micro-sized Al and Zr metal powders via pulsed laser ablation in liquids (PLAL) technique with operating conditions of 532 nm wavelength, 10 Hz frequency and 5 ns pulsed duration . The prepared metal oxides were successfully characterized using various analytical techniques like XRD, SEM, FE-SEM, EDS, TEM, XPS, Uv-Vis spectrophotometer, TGA and FT-IR. De-ionized water was used as a medium of ablation for the synthesis of Al_2O_3 while ZrO_2 was synthesized in three different liquid environments (de-ionized water, ethanol and acetone) to observe the effects of these media on the physical and chemical properties of ZrO_2 nanoparticles produced. The phase transformation as a function of temperature was investigated for the nanocrystal line Al_2O_3 produced. It was observed that the phase transformation $\gamma \rightarrow \alpha - Al_2O_3$ takes place in three steps as evidenced from X-ray diffraction (XRD) and transmission electron microscopy (TEM) studies. The first stage constitutes as-prepared Al_2O_3 and at the temperature of 600^0C which are mixtures of γ- and α- Al_2O_3 phases. The second stage is in the temperature range of 700-900^0C that constitutes pure γ- Al_2O_3 as observed from the XRD patterns, with a cubic crystal structure. The last stage occurs in the temperature of 1000^0C and above, constituted pure α- Al_2O_3 as evidenced from XRD patterns, with corundum crystal structure. It can be concluded from the results obtained from XRD and SAED studies that the crystallinity of the sample increases as the temperature increases. It is also

worth mentioning that the crystallite size calculated from XRD results is closely related to the phase transformation, *i.e*. crystallite size increases with respect to the changes in Al_2O_3 phases and consequently, with the rise in temperature.

Besides, the synthesized ZrO_2 nanoparticles were characterized using various analytical techniques to confirm its structure, compositions and other related properties like optical. XRD analysis confirmed the formation of mixed phases of zirconia (monoclinic and tetragonal) in the three aqueous environments. FT-IR also confirm the formation of ZrO_2 nanoparticles in the three liquids as well the molecular nature and functional groups present in the fabricated ZrO_2. We also emploed XPS technique to prove the composition of the prepared ZrO_2. Uv-Vis absorption spectroscopy analysis was aslo carried out to confirm the rate of absorption of each liquids and also evaluted the band gap of ZrO_2. It was observed that water has highest reflectance and consequently, highest rate of absorption and lower ablation efficiency compared to ethanol and acetone. However, with reference to our findings in XRD and XPS analysis in this research, pure zirconia can be easily produced in water than in ethanol and acetone. The band gap of ZrO_2 produced in the three liquid media was evaluated to be 5.19 eV, 5.22 eV and 4.94 eV in de-ionized water, ethanol and acetone accordingly from Tauc's equation from Uv-Vis absorption spectroscopy. And finally, the morphology of the fabricated ZrO_2 nanoparticles was investigated using TEM analysis which confirms that the nanoparticles produced are spherical in shape and their size is in the range of ~10 nm- 50 nm.

5.2 RECOMMENDATIONS

The following are recommended for future research:

- Othe factors that can affect the compositon and morphology of NPs like wavelenghtand irradiation time could be inestigated for Al2O3 and ZrO2
- Effects of another liquid medium could also be studied for Al and Zr metals
- Other metals could also be studied using the same experimental conditions in this work.
- The applications of these NPs (Al2O3 and ZrO2) in different areas could also be investigated. For instance, gamma alumina can serve as a good catalyst due to its large surface area and polycrystalline α-Al_2O_3 can be used for ceramic applications among many other uses. Also, ZrO_2 when doped with material like MgO could also serve a good catalyst.

References

1. R. feymann, There's plenty of room at the bottom, Miniaturization, edited by H.D.Gilbert, Reinhold, New York, 1961
2. K. Eric Drexler, Engine of creation: the coming era of nanotechnology, ISBN 0-385-19973-2, 1986.
3. Gelperina, K. Kisich, m.D. Iseman and L. Heifets, *Am J respire* crit care Med. **172(12)** (2005) 1487-90.
4. M. F. Hochella, S. K. Lower, P.A. Maurice, R.L. Penn, N. Sahai , D.L. Sparks and B.S. Twining , *Science.* **21(319)** (2008)1631-5.
5. C.P. Poole, F.J. Owens, Introduction to Nanotechnology, Wiley and Sons, 2003.
6. M. Di Ventra, Introduction to Nanoscale Science and Technology, Springer, 2004
7. R.W. Kelsall, I.W. hamley, M. Geoghegan, Nanoscale and Science Technology, John Wiley and Sons, 2005.
8. V. Piriyawong, P.Thongpool Assnithi and P. Limsuwan, *Surface Science Direct*, **32**(2012)1107-1112.
9. S.J. Shaw, W.P. Schiffers, T.P.Gentry and D.C. Emmony, *J. Phys. D,* **32** (1999)1612.
10. H. Cheng, J. Ma, Z. Zhao and L. Qi, *Chem. Mater.* ***7*** (1995) 663-671.
11. S. Ge, X. Shi, K. Sun, C. Li, C. Uher, J.R. Baker, J.M.M.B. Holl and B.G. Orr, *J. Phys. Chem. C* **113** (2009) 13593-13599.
12. Y. Kitamura, N. Okinaka, T. Shibayama, O.O.P. Mahaney, D. Kusano, B. Ohtani and T. Akiyama, *Powder Technology* **176** (2007) 93-98.
13. S. Watson, D. Beydoun, J. Scott and R. Amal, *J. Nanopart. Res*. **6** (2004) 193-207.

14. A. C. Jones and P. R. Chalker, *J. Phys. D: Appl. Phys*. **36** (2003) R80-R95.

15. W. Wang, I. W. Lenggoro, Y. Terashi, T. O. Kim and K. Okuyama, *Mat. Sci. Eng. B* **123** (2005) 194-202.

16. K. Nagaveni, M. S. Hedge, N. Ravishankar, G. N. Subbanna and G. Madras, *Langmuir* **20** (2004) 2900-2907.

17. K. Nagaveni, G. Sivalingam, M. S. Hegde and G. Madras, *Appl. Catal. B* **48** (2004) 83-93.

18. O. Carp, C. L. Huisman and A. Reller, *Progress in Solid State Chem*. **32** (2004) 33-177.

19. X. Chen and S. S. Mao, *Chem. Rev*. **107** (2007) 2891-2959.

20. J. Yang, S. Mei and J. M. F. Ferreira, *Mater. Sci. Eng. C* **15** (2001) 183-185.

21. K. J. Rao, B. Vaidhyanathan, M. Ganguli and P. A. Ramakrishnan, *Chem. Mater.* **11** (1999) 882-895.

22. M. H. Bhat, B. P. Chakravarthy, P. A. Ramakrishnan, A. Levasseur and K. J. Rao, *Bull. Mater. Sci.* **23** (2000) 461.

23. V. Subramanian, C. L. Chen, H. S. Chou and G. T. K. Fey, *J. Mater. Chem*.**11** (2001) 3348-3353.

24. C.J. Brinker, S.W. Scherer, Sol–Gel science: the physics and chemistry of sol–gel processing. Academic Press, New York, 1990.

25. C.J. Brinker, B.C. Bunker, D.R. Tallant, K.J. Ward and R.J. Kirkpatrick, Structure of Sol-Gel Derived Inorganic Polymers: Silicates and Borates, ACS Symposium series, Chapter 26, Vol. 360 (1988) 314-332.

26. R.W. Jones, Fundamental Principles of Sol-Gel Technology, Institute of metals, London (1989).

27. O. Azzaroni, M. Fonticelli, P.L. Schilardi, G. Benitez, I. Caretti, J.M. Albella, R. Gago, L. Vazquez and R.C. Salvarezza, *Nanotechnology* **15** (2004) S197-S200.

28. O. Carp, C. L. Huisman and A. Reller, *Progress in Solid State Chem*. **32** (2004) 33-177.

29. J. Will, A. Mitterdorfer, C. Kleinlogel, D. Perednis, and L.J. Gauckler, *Solid. Stat. Ionics*, **131** (2000) p.79.

30. K.Y. Niu, J. yang, J. Sun and X. W. Du, *Nanotechnology* **21** (2010) 295604.

31. F. Lin, J. Yang, S. H. Lu, K.Y. Niu, Y. Liu, J. Sun and X. W. Du, *J. Matter. Chem*. **20** (2010) 1103-1106.

32 K. Y. Niu, J. Yang, S.A. Kulinich, J. Sun and X. W. Du, *Lanmuir* **26** (2010) 16652-1665.

33 A.S. Loir, F. Garrelie, C. Donnet, M. Belin, Forest B, F. Rogemond, P. Laporte, *Thin Solid Films* **453**(2004) 531.

34 A. S. Loir, F. Garrelie, C. Donnet, M. Belin, B. Forest, F. Rogemond and P. Laporte, *Thin Solid Films* **453**(2004) 531.

35 P.P.Patil, D. M. Phase, S. A. Kulkarni, S.V. Ghaisas, S.K. Kulkarni, S.M. Kanetkar , S. B. Ogale and V.G. Bhide, *Phys. Rev. Lett*. **58**(1987)238.

36 Ogale S B, *Thin Solid Films* **163(**1988) 215.

37 Q. A. Drmosh, S. G. Rao, Z. H. Yamani, M. A. Gondal , Crystalline Nanostructured Cu Doped ZnO Thin Films Deposited at Room Temperature by Pulsed Laser Deposition Technique and Their Characterization, *Appl. Surface Science* 270(2013)104-108.

38 M. A. Gondal, T.F. Qahtan, M.A. Dastageer, M.Y. Maganda and D. H. Anjum, *Appl. Surf. Science* **286** (2013) 149– 155.

39 G.A. Shafeev, E. Freysz and F. Bozon-Verduraz, *Appl. Phys. A,* **78**(2004)307.

40 J.P. Sylvestre, S. Poulin, A.V. Kabashin, E.Sacher, M. Meunier and J.H.T. Luong, *J. Phys. Chem. B,* **108**(2004)16864.

41 M. Sugiyama, H. Okazaki and S. Koda, J. *Appl. Phys*.**41**(2002) 4666.

42 J.W. Chen, Q.Z. Dong, J.Yang, Z.X. Guo, Z.L. Song and J.S. Lian, *Mater. Lett.* **58**(2004)337.

43 S.I. Dolgaev, A.V. Simakin, V.V. Voronov, G.A. Shafeev and F. Bozon-Verduraz, *Appl. Surf. Sci.* **186**(2002)546.

44 T. Tsuji, T. Hamagami, T. Kawamura, J. Yamaki and M. Tsuji, *Appl. Surf. Sci*. **243**(2005)214.

45 J.B. Wang and G.W. Yang, *Appl. Phys. A*, **71**(2000) 343.

46 C.H. Liang, Y.Shimizu, M. Masuda, T.Sasaki and N.Koshizaki , *Chem. Mater.*, 16 (2004) 963.

47 H. Usui, T. Sasaki and N. Koshizaki, *Chem. Lett.,* **34** (2005)700.

48 H.B. Zeng, W.P. Cai, B.Q Cao, J.L.Hu, Y. Li, P.S.Liu, *Appl. Phys. Lett*., 88 (2006) 181905.

49 V. Amendola and M. Meneghetti, *Physical Chemistry Chemical Physics*, **11** (2009) 3805-3821.

50 I. Srnová, M. Procházka, B. Vlčková, J. Štěpánek and P. Malý, *Langmuir*, **14(16)** (1998)4666-4670.

51 J.P. Sylvestre, S. Poulin, A.V. Kabashin, E. Sacher, M. Meunier and J.H.T. Luong, *J.Phys.Chem. B,* **108** (2004)16864-16869.

52 Y. Takeda, T. Kondow and F. Mafune, *Nucleoside, Nucleotides, and Nucleic Acids,* **24(8)** (2005) 1215-1225.

53 G.W. C.Y. Zang, X.L. Zhang and Z.H.A. Zhong, *Chem. Phys. Lett*., **367**(2003)10.

54 J.B. Wang, C.Y. Zhang, X.L. Zhong and G.W. Yang, *Chem. Phys. Lett*., **86** (2002) 361.

55 L. Yang, P.W. May, L. Yin, J.A. Smith and K.N. Rosser, *Diamond Relat. Mater*. **16**(2007)725.

56 P. Politzer, P. Lane and M.E. Grice,. *Journal of Physical Chemistry A* **105 (31)** (2001**)** 7473-7480.

57 H. Ritter, S. Braun, *Propellants Explosives Pyrotechnics* **26(6)** (2001)311-314.

58 J.A. Rodriguez, M. Fernandez-Gercia, (Eds) *Synthesis, properties and Applications of oxide Nanoparticles. Wiley: New Jersey, 2007*

59 G.C. Mather, A.Martinez Arias, *Transport* properties and oxygen handling in "Synthesis, Properties and Applications of oxide materials" (Rodiguez, *J.A., Fernandez-Garcia,* M; Eds). Wiley: N.J., 2007 Chapt. 13.

60 H.C. Stumpf, A.S. Ressel, J.W. Newsome and C.M. Tucker, *Ind. Eng. Chem,* **42**(1950)1398.

61 J.M. McHale, A. Auroux, A.J. Perrota and A. Navrotsky, *Science,* **277**(1997)788.

62 H. Knozinger and P. Ratnasamy, *Catl. Rev. Sci. Eng.,* **17**(1978)31

63 G. Busca, *The surface acidity and basicity of solid oxides and zeolites* in "Metal oxides" (Fierro, J.L.G.; Ed). CRC, Boca Raton,2006

64 Y.Wang, C. Bryan, H. Xu, P. Pohl, Y.Yang and C.J. Brinker, *J Colloid Interf. Sci*. ***23(***2002) 254.

65 S. H. Cai, S.N. Rashkeev, S.T. Pantelides and K. Sohlberg, *Phys. Rev.* B 67(2003) 224104.

66 T. Tsuji, D.H. Thang, Y. Okazaki, M. Nakanishi, Y. Tsuboi and M. Tsuji, *Applied surface Science* **254**(2008) 5224-5230.

67 S. Cava, S.M. Tebcherani, I.A. Souza, S.A. Pianaro, C.A. Paskocimas, E. Longo and J.A. Varela, *Materials Chemistry and Physics,* **103** (2007) 394-399.

68 V. Piriyawong, V. Thongpool, P. Asanthi, and P. Limsuwan, *J. Nanomater,* **2012, (**2012) 819403.

69 Dehzi Tang, Geng Lin, Yin Liu, Yu Teng, Yixi Zhuang, Bin Zhau, Quanzhong Zhao and Jianrong Qiu, *J Nanooart Res* **13** (2011) 1183-1190.

70 G. Dercz, Prusik, and L. Pajak, *Journal of Achievement in Materials and Manufacturing Engineering,* 31(2008)408-414

71 .A.K. Singh and Umesh T. Nakate, *The Scientific World Journal*, (2014) 349457. http://dx.do.org/10.1155/2014/349457.

72 W. Callister, *Materials Science and Engineering, an introduction,* 7 th ed. New York: John Wiley &Sons, Inc, 2007.

73 A.H. Heuer and L.W. Hobbs (eds.), *Science and Technology of Zirconia, Advances in Ceramics,* Vol.3. (The American Ceramics Society, Westerville, OH, 1981)

74 B.C.H. Steele and A. Heinzel, *Nature* **414**(*2001)*345.

75 A.D. Brailsford, E.M. Logothetis, *Sensors and Actuators B* **52**(1998)195.

76 S.I. Somov, G. Reinhardt, U. Guth, W. Gopel, *Solid State Ionics* **543**(2000)136-137.

77 W. Stichert, F. Shuth, *Chem. Mater.* **10***(*1998)2020.

78 M. W. Finnis, A.T. Paxton, M. Methfessel and M. van Schilfgaarde, *Phys. Rev. Lett*. **81**(1998)5149.

79 P. Bouvier, J. Godlewski and G. Lucazeau, *J. Nucl. Mater*. **300**(2002)118.

80 M. Gateshki, V. Petkov, G. Williams, S.K. Pradhan and Y. Ren, *Phys. Rev. B* **71**(2005)224107.

81 G. Pacheco and J.J. Fripiat, *J. Phys. Chem. B* **104**(2000)11906.

82 M. J. Mayo, A. Suresh and W.D. Porter, *Rev. Adv. Mater. Sci*. **5**(2003)100.

83 S. Xie, E. Iglesia and A.T. Bell, *Chem. Mater.* **12**(2000)2442.

84 R. Srinivasan, T.R. Watkins, C.R. Hubbard and B.H. Davis, *Chem. Mater*. 7 (1995)725.

85 S. Chang and R. Doong, *Chem. Mater*. 17 (2005) 4837.

86 A.V. Chadwick, G. Mountjoy, V.M. Nield, I.J. F. Poplett, M.E. Smith, J. H. Strange and M.G. Tucker, *Chem. Mater.* **13**(2001)1219.

87 M. Fernández-García, A. Martínez-Arias, J.C. Hanson and J.A. Rodríguez, *Chem. Rev.* **104**(2004)4063.

88 G. Adachi, N. Imanaka and S. Tamura, Chem. *Rev.* **102**(2002)2405.

89 J. C. Garcia, L.M.R. Scolfaro and A.T. Lino, *Journal of Applied Physics,* **100(10)** (2006)104103.

90 J.C. Garcia, L.M.R. Scolfaro and A.T. Lino, *Journal of Applied Physics,* **100** (2006)10.

91 Michael Eshed, Swati Pol, Aharon Gedanken and Mahalingam Balasubramanian, *Beilstein Journal of Nanotechnology*, **2** (2011) 198-203.

92 Mohammed Rafiq Hussain Siddiqui, Abdulaziz Ibrahim Al-Wassil, Abdullah Mohammed Al-Otaibi and Refaat Mohammed Mahfouz, *Materials Research*, **15(6)** (2012) 986-989.

93 Bambang Sunendar Purwasasmita, Lucyana Dwi Larasati, Rifki Septawendar, Ashari Budi Nugraha, Muhammed Rifqi Aufan, and Harini Sosiati, *Journal of the Australian Ceramic Society Volume* **49(2)** (2013) 89-94.

94 D.S.S. Padovini, D.S.L. Pontes, C.J. Dalmaschio, F.M. Pontes, and E. Longo, *RSC Adv.* **4** (2014) 38484-38490.

95 Adel K. Mahmoud, Zainab Fadhill, Suha Ibrahim Al-nassar, Furat Ibrahim Husein, Erhan Akman, and Arif Demir, *Journal of Material Science and Engineering B* **3(6)** (2013) 364-368.

96 Mahdieh Mohammad Hossein and Fattahi Behzad, *Applied Surface Science,* **329** (2015)47-57.

97 W. Friedrich, P. Knipping, M.V. Laue, Acad. *Wissen Munich*. **303** (1912) 6.

98 D. Liu, Q. Wang, H.L.M. Chang and H. Chen, *J. Mater. Res*. **10** (1995) 1516.

99 C. Richard, A. Jr. Charles, and S. Wilson, Encyclopedia of Materials Characterization - Surfaces, Interfaces, Thin Films, Elsevier (1992).

100 Fabrication and characterization of metal oxide nanostrutures submitted by Li Dan, University of Hong Kong, July (2007).

101 Transmission Electron Microscopy and Diffractometry of Materials, Springer, ISBN 3540738851 (2007).

102 P. E. Champness, Electron Diffraction in the Transmission Electron Microscope, Garland Science, ISBN 1859961479 (2001).

103 A. Hubbard, The Handbook of surface imaging and visualization, CRC Press. ISBN 0849389119 (1995).

104 B. J. Clark, T. Frost, and M. A. Russell, UV spectroscopy: techniques, instrumentation, data handling, Chapman & Hall, London, UK (1993).

105 H. H. Perkampus, UV-VIS spectroscopy and its applications, Springer-Verlag, Berlin, Germany (1992).

106 P. W. Atkins and J. de Paula, Atkins Physical Chemistry, 7th ed. Oxford University Press, New York, USA (2002).

107 P. W. Atkins and R. S. Friedman, Molecular Quantum Mechanics, 3rd ed. Oxford University Press, New York, USA (1997).

108 X. Michalet, F. Pinaud, T. D. Lacoste, M. Dahan, M. P. Bruchez, A. P. Alivisatos, and S. Weiss, *Single Molecules* **2** (2001) 261-276.

109 D. N. Kendall, Applied infrared spectroscopy, Reinhold Pub. Corp. New York, USA (1966).

110 H. W. Siesler and K. Holland-Moritz, Infrared and Raman spectroscopy of polymers, M. Dekker, New York, USA (1980).

111Nanoscale Science and Technology, edited by R. Kelsall, I. Hamley, M. Geoghegan, John Wiley and Sons, Ltd. (2005).

112 H. Kao, R. Wu, T.Chen and C. Yeh, *J. Mater. Chem.*, **10** (2000) 2802.

113 R.K. Pati, J.C. Ray and P. Pramanik, *Mater. Lett*. **44 (**2000) 299-303.

114 P.L. Chang, F.S. Yen, K.C. Cheng and H.L. Wen, *Nano Lett.* **1 (5) (**2001)253-261.

115 J. McHale, A. Auroux, A. perrota and A Navrotsky, *Science*, **277 (**1997)788.

116 H.K. Varma, T.V. Mani and A.D. Damodran, *J. Am. Ceram. Soc.* **77 (**1994)1597-1600.

117 J. Li, Y. Pan, Xiang, Q. Ge and J. Guo, *Ceram. Intern.* **32 (**2006)587-591.

118 F. Mirjalili, H. Mohamad, and L. Chuah, *Ceramics – Silikáty* **55 (4)** (2011)378-383.

119 O. Bose, E. Kemnitz, A. Lippitz, and W.E.S. Unger, Fresenius *J. Anal. Chem*. **358 (**1997)175-179.

120 S. Thomas, and P.M.A. Sherwood, *Anal. Chem.* **64 (**1992) 2488.

121 C. D. Wanger, W. M. Riggs, L. E. Davis, J. F. Moulder and G. E.Muilenberg, *Handbook of Handbook of X-ray Photoelectron Spectroscopy, Perkin Elmer Corporation*, 1979, page 213.

122 L.A. Perez-Maqueda and E. Matijevic, *Journal of Materials Research*, **12** (1997) 3286-3292.

123 R.C. Garvie, *Journal of Physical Chemistry*, **69 (4)** (1965) 1238-1243.

124 Misun Chun, Myung-Jun Moon, Juyun Park and Young-Heol Kang, *Bull. Korean Chem. Soc.* **30**(2009)11.

125 Shou-Yong Jing, Heon-Ju Lee and Chi Kyu Choi, *Journal of the Korean Physical Society*, **41(5)** (2002)769-773.

126 S.Z. Khan, Y.D. Yuan, A.Abdolvand, M. Schmidt, P. Crouse and L.Li, *Journal of Nanopart. Res.* **11** (2008) 1421-1427.

127 J. A. Creighton and D. G. Eadon, *J. Chem. Soc. Faraday Trans.* **87** (1991) 3881.

128 C.M. Phillippi and K.S. Mazdyasni, *J. Am. Ceram. Soc.* **54** (1971) 254-259.

129 Y. Gao, Y. Masuda, W.S. Seo, H. Ohta and K. Koumoto, *Ceram.Int.* **30** (2004) 1365-1368.

130 C. Li and M. Li, *J. Raman Spectrosc.*, **33** (2002) 301-308.

131 M. Taguchi, S. Takami, T. Adschiri, T. Nakane, K. Sato and T. Naka, *CrystEngComm*, **14** (2012) 2117-2123.

132 D. Sarkar, D. Mohapatra, S. Ray, S. Bhattacharyya, S. Adak and N. Mitra, *Ceram. Int.*, **33** (2007) 1275-1282

133 Y.M. Wang, Y.S. Li, P.C. Wong, K.A.R. Michell, *Applied Surface Science* **72** (1993) 237-244.

134 V. Maurice, M. Salmeron and G.A. Somojai, *Surf. Sci*. **237** (1990) 116.

135 J. Rheims, J. Koser, T. Wried, *Meas. Sci. Technol.* **8** (1997) 601–605.

136 S.C. Singh, H. Zeng, C. Guo, W. Cal, *Nanomaterials: Processing and Characterization with Lasers*(First Ediation)Wiley-VCH Verlag GmbH & Co, KGaA(2012)

137 J.A. Creighton, D.G. Eadon, *Journal of the Chemical Society-Faraday Transactions*

Vitae

Name	Fasasi Teslim Ayinde
Nationality	Nigerian
Date of Birth	02-06-1982
E-mail	fasas03@yahoo.com
Address	Olunde via Lagos-Ibadan Express way, Ibadan, Nigeria.
Academic background	B.Tech Pure and Applied Physics, Ladoke Akintola University of Technology, Ogbomoso, Nigeria.

PUBLICATIONS AND CONFERENCES

1. M.A. Gondal, A.M. Ilyas, **T.A. Fasasi**, M.A. Dastageer, Z.S. Seddigi, T.F. Qahtan, M. Faiz, G.D. Khattak, Synthesis of Green TiO_2/ZnO/CdS Hybrid Nano-catalyst for Efficient Light Harvesting using an Elegant Pulsed Laser Ablation in Liquids Method, Applied Surface Science (2015), http://dx.doi.org/10.1016/j.apsusc.2015.09.213.
2. M. A. Gondala, **T. A. Fasasi**, A. Mekki, T.A. Saleh, A.M Ilyas, T.F. Qahtan, X.Chang , Phase Transformation and Structural Characterization Studies of Aluminum Oxide (Al_2O_3) Nanoparticles Synthesized using Pulsed Laser Ablation in Liquids Elegant Method, Applied Surface Science (2015) (Revised version submitted).

3. **T. A. Fasasi,** M.A. Gondal, A. Mekki, A. M. Ilyas, T.F Qahtan, Effects of Oxidizing Media on the Composition, Morphology and Optical properties of colloidal Zirconium Oxide (ZrO_2) Nano particles Synthesized via Pulsed laser ablation (PLA) in liquids Technique (Submitted).
4. M.A. Gondal, **T.A. Fasasi**, A. M. Ilyas, M.A. Dastageer, T. F. Qahtan (2015) Synthesis and Characterization of Phase Transition of Al_2O_3 Nanoparticles Via Pulsed Laser Ablation in Liquids, Interantional Conference on Atmoic, Molecular and Optical Physics (AMOP), Al-Jouf, Saudi Arabia (31st march - 2ndApril, 2015).
5. M.A Gondal, A.M. Ilyas, **T.A. Fasasi**, M.A. dastageer, T.F. Qahtan (2015) Synthesis of Ag-ZnO Core-Shell Composite Structures Using Pulsed laser ablation in Liquids (PLAL) for Visible Light Applications, International Conference on Atomic, Molecular and Optical Physics (AMOP), Al-jouf, Saudi Arabia (31^{st} March-2^{nd} April, 2015).